



Introduction to the NJIAS Himawari-8/9 cloud feature dataset for climate and typhoon research

Xiaoyong Zhuge¹, Xiaolei Zou², Lu Yu¹, Xin Li¹, Mingjian Zeng¹, Yilun Chen³, Bing Zhang¹, Bin Yao¹, Fei Tang¹, Fengjiao Chen¹, Wanlin Kan¹

5 ¹Key Laboratory of Transportation Meteorology of CMA, Nanjing Joint Institute for Atmospheric Sciences, Nanjing, 210041, China

²Joint Center of Data Assimilation for Research and Application, Nanjing University of Information Science and Technology, Nanjing, 210044, China

³School of Atmospheric Sciences, Sun Yat-sen University, Zhuhai, 519082, China

10 *Correspondence to:* Xiaolei Zou (xzou@nuist.edu.cn)

Abstract. The use of remote sensing method to accurately measure cloud properties and their spatiotemporal changes has been widely welcomed in many fields of atmospheric research. The Nanjing Joint Institute for Atmospheric Sciences (NJIAS) Himawari-8/9 Cloud Feature Dataset (HCFD) provides a comprehensive description of cloud features over the East Asia and west North Pacific regions for the

15 7 yr period from April 2016 to December 2022. Multiple cloud variables, such as cloud mask, phase/type, top height, optical thickness, and particle effective radius, as well as snow, dust and haze masks, were generated from the visible and infrared measurements of the Advanced Himawari Imager (AHI) onboard the Japanese geostationary satellites Himawari-8/9 using a series of cloud retrieval algorithms developed by Dr. Zhuge and his colleagues. Verifications with the *Cloud–Aerosol Lidar with Orthogonal*

20 *Polarization* 1-km cloud layer product and the *Moderate Resolution Imaging Spectroradiometer* Level-2 cloud product (MYD06) demonstrates that the NJIAS HCFD gives higher skill scores than the Japanese Himawari-8/9 operational cloud product for all cloud variables except for the particle effective radius. The NJIAS HCFD even outperforms the MYD06 in the nighttime continental cloud detection and the infrared-only cloud-top phase determination. Then, two application examples are presented, to

25 demonstrate the use of the NJIAS HCFD for climate and typhoon research. The NJIAS HCFD has been published at the Science Data Bank (<https://doi.org/10.57760/sciencedb.09950>, Zhuge 2023a; <https://doi.org/10.57760/sciencedb.09953>, Zhuge 2023b; <https://doi.org/10.57760/sciencedb.09954>, Zhuge 2023c; <https://doi.org/10.57760/sciencedb.10158>, Zhuge 2023d; <https://doi.org/10.57760/sciencedb.09945>, Zhuge 2023e).

30



1 Introduction

Clouds play a crucial role in severe weather systems. The formation, development, and dissipation of convective storms are closely related to cloud microphysical processes (Zhuge and Zou, 2018; Liu et al., 2020). The intensity and size of a tropical cyclones are also indicated by the states of clouds (Zhuge et al., 2015; Sun et al., 2021). In addition, clouds modulate the planetary radiation budget by reflecting incoming solar radiation and absorbing outgoing long-wave radiation in Earth's climate system (Stephens, 2005; Yang et al., 2015) and affect the Earth's hydrological cycle by altering the water distribution through precipitation (Rosenfeld et al., 2014; Stevens and Bony, 2013). However, cloud processes are not yet well understood nor accurately predicted by current weather and climate models. Obtaining global cloud properties and their spatiotemporal changes has always been of great interest to weather and climate community at large.

Satellite remote sensing is an approach to observe and retrieve cloud properties on a global scale. There are two types of satellite sensors: active and passive sensors. Active sensors, such as the Cloud-Aerosol Lidar with Orthogonal Polarization (CALIOP) onboard the Cloud-Aerosol Lidar and Infrared Pathfinder Satellite Observation satellite (Winker et al., 2007), and the Cloud Profiling Radar onboard the CloudSat satellite (Stephens et al., 2002), can provide cloud profile information at a high spatial resolution with high accuracy. However, these sensors often have limited spatial coverage due to their nadir-only sampling mode. In contrast, the passive sensors provide measurements of wide swaths and multiple channels, which allows cloud top properties be retrieved over a large-coverage area. For example, the Moderate Resolution Imaging Spectroradiometer (MODIS) onboard the Earth Observing System *Aqua* and *Terra* platforms provide observations that are highly sensitive to cloud. It has 36 channels ranging from visible to infrared (IR) at a nadir spatial resolution of 0.25–1 km (Platnick et al., 2003). The unique spectral and spatial capabilities give birth to MODIS Level-2 cloud products (known as MOD06 for *Terra* and MYD06 for *Aqua*) which have been proven to have high accuracy and are widely used within the earth system science research community. Due to the safety concerns arising from MODIS extended service life, the National Aeronautics and Space Administration (NASA) is promoting a migration project to apply the MYD06 algorithms to the Visible Infrared Imaging Radiometer Suite (VIIRS) onboard the U.S. polar-orbiting operational environmental satellites (Platnick et al., 2021). However, both MODIS and VIIRS have a revisit interval of 1-2 days, which means that the temporal



60 evolution of clouds cannot be captured by these instruments.

The new generation of geostationary satellite imagers, such as the Advanced Himawari Imager (AHI) onboard Japanese Himawari-8/9 satellites (Bessho et al. 2016), the Advanced Baseline Imager (ABI) onboard U.S. Geostationary Operational Environmental Satellite (GOES)-R series (Schmit et al., 2017), the Advanced Geostationary Radiation Imager onboard Chinese Fengyun-4 satellites (Yang et al., 65 2017), and the Flexible Combined Imager onboard European Meteosat Third Generation (Holmlund et al. 2021), can continuously observe large-scale regions at a high spatiotemporal resolution. This capability enables a comprehensive remote sensing of various cloud properties.

The GOES-R Algorithm Working Group has developed a series of retrieval algorithms for ABI cloud (Heidinger and Straka, 2013) and fog (Calvert and Pavolonis, 2010) masks, cloud height (Heidinger, 70 2012), cloud phase and type (Pavolonis, 2010), as well as daytime (Walther et al., 2013) and nighttime (Minnis and Heck, 2012) optical/microphysical parameters. For AHI official cloud algorithms, the techniques developed by Ishida and Nakajima (2009) and Nakajima et al. (2011) are used for the AHI cloud mask and phase determinations and a multifunctional algorithm called *Comprehensive Analysis Program for Cloud Optical Measurement* is employed to retrieve the optical and microphysical 75 parameters for liquid-water (Nakajima and Nakajima, 1995; Kawamoto et al., 2001) and ice (Letu et al., 2019, 2020) clouds. The AHI level-2 operational cloud product from September 2015 to the present at a low spatial resolution of $0.05^\circ \times 0.05^\circ$ is archived on the P-Tree System, Japan Aerospace Exploration Agency (JAXA). All cloud variables are available only during the daytime at solar zenith angles below 80° .

80 To supplement the JAXA operational cloud algorithms and products, starting from 2016, the authors have successively developed multiple algorithms for AHI cloud mask (Zhuge and Zou, 2016; Zhuge et al., 2017), cloud-top phase (Zhuge et al., 2021a), cloud type (Zhang et al., 2019; Sun et al., 2019), and daytime cloud optical/microphysical parameters (DCOMPs; Zhuge et al., 2021b). They are now collectively referred to as Nanjing Joint Institute for Atmospheric Sciences (NJIAS) cloud retrieval 85 algorithms. The cloud variables are generated at full and half clocks in the 7 yr period from April 2016 to December 2022 using these algorithms. They are named as the NJIAS Himawari-8/9 Cloud Feature Dataset (HCFD). The objects of this article are twofold: 1) to give an in-depth overview of the NJIAS HCFD, including the updates made to NJIAS cloud retrieval algorithms since 2021; and 2) to objectively evaluate the accuracy of NJIAS HCFD, particularly its comparative performance with existing datasets.



90 The remaining parts of this article are organized as follows. Section 2 gives a detailed overview of
the NJIAS HCFD. Section 3 presents results of an evaluation of the NJIAS HCFD accuracy against the
CALIOP and Collection-6.1 MYD06 datasets. Section 4 presents two application examples: one on cloud
climatology in southwestern China and the other on cloud and precipitation features of landfalling
typhoons. After a description on data availability (section 5), a summary and conclusions are given in
95 section 6.

2 Overview of the NJIAS HCFD

2.1 Input data

The primary sensor data employed by the NJIAS HCFD are the multispectral observations of the
AHI onboard Himawari-8/9. Himawari-8 became operational on July 7, 2015 and was replaced by its
100 successor, Himawari-9 on December 13, 2022. The AHI provides a full-disk scan every 10 min with a
spatial resolution of 0.5–2 km at the sub-satellite point around 140.7°E. During the data dissemination
step, AHI full disk imagery is divided into ten segments from north to south by the Japan Meteorological
Agency. The NJIAS HCFD only focuses on Segments 2–4, covering the vast majority of the East Asia
and western North Pacific (WNP) regions. Given that the AHI IR channels have coarser spatial
105 resolutions (2 km) than the visible and shortwave-IR (SWIR) ones (0.5–1 km), data from finer-resolution
channels are each aggregated to 2 km resolution.

Clear-sky brightness temperatures (BTs) and transmission profiles for AHI 10 IR channels are
simulated by using the Community Radiative Transfer Model (CRTM) of version 2.2.3 (Han et al., 2007)
with the vertical profiles of pressure, temperature, water vapor and composition, as well as surface
110 variables of surface skin temperature and 10-m wind, from the U.S. National Centers for Environmental
Prediction (NCEP) Final operational global (FNL) analyses (Kalnay et al., 1996) as the input. The NCEP
FNL analysis has a $0.25^\circ \times 0.25^\circ$ horizontal resolution and a 6-h interval. Other ancillary data including
surface type, terrestrial elevation, and land surface emissivity are extracted from the one-minute land
ecosystem classification product (<http://modis-atmos.gsfc.nasa.gov/ECOSYSTEM/index.html>), global
115 30 arc-second elevation dataset (http://webmap.ornl.gov/ogcdown/dataset.jsp?ds_id510003), and
University of Wisconsin–Madison High Spectral Resolution Emissivity dataset
(<http://cimss.ssec.wisc.edu/iremis>), respectively.



Table 1: List of output variables.

Short name	Long name	Assigned value or Unit
CldMask	Cloud mask	Confidently clear=0; Probably clear=1; Probably cloudy=2; Confidently cloudy=3
FogMask	Fog/Low stratus mask	Probably Foggy = 1; Confidently foggy = 2
CldType	Cloud type	Confidently clear=0; Probably clear=1; Broken=2; Warm water = 3; Supercooled water = 4; Mixed = 5; Opaque Ice = 6; Cirrus = 7; Overlapped = 8; Overshooting = 9
CldType2	Cloud type in ISCCP rule ¹	Confidently clear=0; Probably clear=1; Broken=2; Cu = 3; Sc = 4; St = 5; Ac = 6; As = 7; Ns = 8; Ci = 9; Cs=10; Cb=11
CldPhase	Cloud-top thermodynamic phase	Clear =0; Warm-water = 1; Supercooled-water = 2; Mixed/uncertain = 3; Ice = 4
CldTemperature	Cloud-top temperature	K
CldHeight	Cloud-top height	m AGL
CldPressure	Cloud-top pressure	hPa
ACHA_COD	Cloud optical thickness from the ACHA approach ²	unitless
ACHA_CPS	Cloud-top particle effective radius from ACHA the approach ²	μm
DCOMP*_COD ³	Cloud optical thickness from the DCOMP approach ¹	unitless
DCOMP*_CPS ³	Cloud-top particle effective radius from the DCOMP approach ¹	μm
DCOMP*_LWP ³	Cloud liquid water path from the DCOMP approach ¹	g m ⁻²
DCOMP*_IWP ³	Cloud ice water path from the DCOMP approach ¹	g m ⁻²
LatPC	Latitude after parallax corrections	° N
LonPC	Longitude after parallax corrections	° E
SST	Clear-sky sea skin temperature	K
ShadowMask	Shadow ¹	Shallow=1
HazeMask	Haze ¹	Haze=1
SnowMask	Snow and sea-ice surface ¹	Snow/Ice = 1; Permanent snow = 2
FireMask	Active fire	Possible fire=1; Confident fire=2
DustMask	Dust	Possible dust=1; Confident dust=2

¹ Daytime only.

120 ² Only reliable for cirrus clouds.

³ DCOMP* represents DCOMP35, DCOMP36 and DCOMP37, meaning the variables are derived using 0.64-μm and either 1.6-, 2.3-, or 3.9-μm channels, respectively.

2.2 Output variables

125 The NJIAS HCFD provides a comprehensive description of cloud features over the East Asia and WNP regions. It includes 30 variables, such as cloud mask, cloud optical thickness (τ), cloud-top thermodynamic phase, cloud-top height (CTH), and cloud-top particle effective radius (R_e), as well as snow, dust and haze masks. The 30 output variables are briefly described in Table 1.



2.3 NJIAS cloud retrieval algorithms

130 During the past three years, a number of improvements to the NJIAS cloud retrieval algorithms
have been incorporated. Improvements include the following.

2.3.1 Cloud mask algorithm refinements

The NJIAS cloud mask algorithm is developed on the basis of previous two works (Zhuge and Zou,
2016; Zhuge et al., 2017). Eight of ten cloud-mask tests used in Zhuge and Zou (2016) and one test used
135 in Zhuge et al. (2017) are inherited. These nine cloud-mask tests are called relative thermal contrast test
(RTCT), emissivity at tropopause test (ETROP), positive channel-14 minus 15 test (PFMFT), relative
channel-14 minus 15 test (RFMFT), cirrus water vapor test (CIRH2O), uniform low stratus test (ULST),
new optically thin cloud test (N-OTC), temporal IR test (TEMPIR), and visible-based cloud index test
(VCI). To enhance the detection of low-level clouds, additional six cloud-mask tests are employed by the
140 NJIAS algorithm, that is, relative visible contrast test (RVCT), reflectance ratio test (RRT), terminator
thermal stability test (TTST), reflectance similarity test (RST), nighttime low stratus test over desert
(DZT_NLS), and daytime low stratus test over sunglint regions (SG_DLS). The mathematical formulas
for the above-mentioned 15 cloud-mask tests are listed in Table 2. Note that $O_{x\mu m}$ is the observed BT
or reflectance at x - μm wavelength, $B_{x\mu m}$ is the simulated x - μm BT under clear-sky conditions,
145 $I_{x\mu m}(T)$ represents the radiance at temperature T and x - μm wavelength that is computed by the
Planck function, and \mathcal{E} is the threshold for a certain test.



Table 2: Names and mathematical formulas for the 15 tests employed by the NJIAS cloud mask algorithm.

Name	Condition for cloudy pixels	Remarks
RTCT	$(O_{11.2\mu m}^{\max} - O_{11.2\mu m}) > \varepsilon_{RTCT}$	Inherited from Zhuge and Zou (2016)
ETROP	$\frac{I_{11.2\mu m}(O_{11.2\mu m}) - I_{11.2\mu m}(B_{11.2\mu m})}{R_{11.2\mu m}^{\text{trop}} - I_{11.2\mu m}(B_{11.2\mu m})} > \varepsilon_{ETROP}$	
PFMFT	$(O_{11.2\mu m} - O_{12.4\mu m}) - (B_{11.2\mu m} - B_{12.4\mu m}) \cdot \frac{(O_{11.2\mu m} - 260K)}{(B_{12.4\mu m} - 260K)} > \varepsilon_{PFMFT}$	
RFMFT	$ (O_{11.2\mu m} - O_{12.4\mu m}) - (O_{11.2\mu m}^{NWC} - O_{12.4\mu m}^{NWC}) > \varepsilon_{RFMFT}$	
CIRH2O	$\rho(O_{11.2\mu m}, O_{7.3\mu m}) > \varepsilon_{CIRH2O}$	
ULST	$\frac{I_{3.9\mu m}(B_{3.9\mu m})}{I_{3.9\mu m}(B_{11.2\mu m})} - \frac{I_{3.9\mu m}(O_{3.9\mu m})}{I_{3.9\mu m}(O_{11.2\mu m})} > \varepsilon_{ULST}$	
N-OTC	$O_{3.9\mu m} - O_{12.4\mu m} > \varepsilon_{N-OTC}$	
TEMPIR	$O_{11.2\mu m}^{-10\text{min}} - O_{11.2\mu m} > \varepsilon_{TEMPIR}$	
VCI	$\sqrt{\frac{(O_{0.47\mu m} - O_{0.64\mu m})^2 + (O_{0.47\mu m} - O_{0.86\mu m})^2 + (O_{0.64\mu m} - O_{0.86\mu m})^2}{3}} < \varepsilon_{VCI}$	Inherited from Zhuge et al. (2017)
RVCT	$O_{0.64\mu m}^{\text{Norm}} - O_{0.64\mu m}^{\text{Norm,min}} > \varepsilon_{M-RVCT}$	Adopted from Heidinger and Straka (2013)
RRT	$\frac{O_{0.86\mu m}}{O_{0.64\mu m}} > \varepsilon_{RRT}$	
TTST	$ O_{11.2\mu m}^{-1hr} - O_{11.2\mu m} < 2$ and $CM^{-1hr} = \text{TRUE}$ and $ (O_{11.2\mu m}^{-1hr} - O_{8.6\mu m}^{-1hr}) - (O_{11.2\mu m} - O_{8.6\mu m}) < \varepsilon_{TTS}$	
RST	$\frac{O_{1.6\mu m}}{O_{0.64\mu m}} > 0.8$ and $O_{1.6\mu m}^{\text{Norm}} > \frac{\theta_{sol}}{300} - 0.05$ and $CM^{\text{Neighbor}} = \text{TRUE}$ and $\frac{O_{0.64\mu m}}{O_{0.64\mu m}^{\text{Neighbor}}} > \varepsilon_{TRS}$	Newly added
SG_DLS	$B_{3.9\mu m} - O_{3.9\mu m} > \varepsilon_{SG_DLS1}$ or $\frac{(O_{3.9\mu m} - O_{10.4\mu m})}{O_{0.64\mu m}} < \varepsilon_{SG_DLS2}$	
DZT_NLS	$O_{12.4\mu m} - O_{10.4\mu m} < 0$ and $(O_{10.4\mu m} - O_{3.9\mu m} + 5)/10 - (O_{12.4\mu m} - O_{10.4\mu m} + 4)/6 > 0.16$ and $\frac{I_{3.9\mu m}(B_{3.9\mu m})}{I_{3.9\mu m}(B_{11.2\mu m})} - \frac{I_{3.9\mu m}(O_{3.9\mu m})}{I_{3.9\mu m}(O_{11.2\mu m})} > \varepsilon_{DZT_NLS}$	

150 Detection of low-level clouds at high solar zenith angles is challenging since the visible reflectance becomes very sensitive to aerosol and noise. To mitigate the labeling of haze pixels as being cloudy, VCI



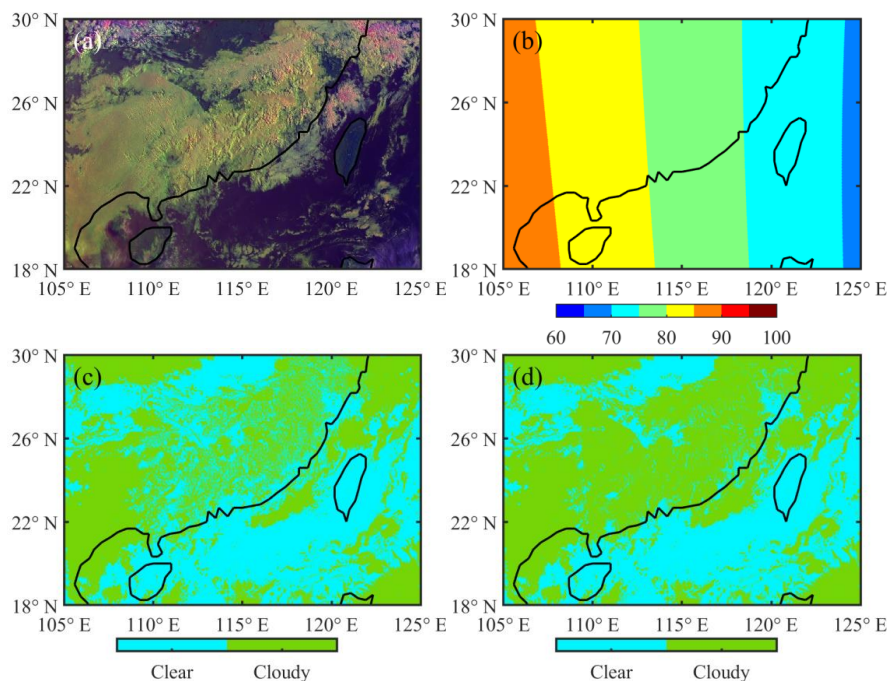
and RRT were slightly modified. The pixels should firstly satisfy two basic conditions
 ($O_{1.6\mu m}^{Norm} > \frac{\theta_{sol}}{300} - 0.05$ and $323 - O_{11.2\mu m} > 150 \cdot O_{1.6\mu m}^{Norm}$) before they could proceed to next step.

Here, θ_{sol} is the solar zenith angle in degree, and $O_{1.6\mu m}^{Norm}$ is the 1.6- μm reflectance normalized by the
 155 cosine of θ_{sol} . Meanwhile, given that existing three reflectance-based tests (i.e., VCI, RVCT, and RRT)
 are not as effective as at noon, TTST and RST are incorporated into the NJIAS cloud mask algorithm to
 improve cloud detection at high solar zenith angles. As described by Heidinger and Straka (2013), TTST
 classifies a pixel as cloudy if its IR spectral signatures are similar to those of a cloudy pixel that was
 detected at the same location one hour ago. RST is a completely new cloud-mask test, being specifically
 160 utilized for pixels with a solar zenith angle between 60° and 83° . The objective of RST is to spatially
 extend the initial cloud “seeds” to their neighboring pixels that exhibit similar reflectance characteristics.

Again, these candidate cloudy pixels should firstly satisfy non-haze conditions ($\frac{O_{1.6\mu m}}{O_{0.64\mu m}} > 0.8$ and
 $O_{1.6\mu m}^{Norm} > \frac{\theta_{sol}}{300} - 0.05$). Figure 1 illustrates the utility of incorporating the RST for low-level cloud
 detection in the early morning. The scene occurred at 23:00 UTC 10 April 2023, when a vast expanse of
 165 quasi-stationary cloud belts were located over southern China. When detecting clouds without RST, a lot
 of foggy and/or stratus pixels were missed, and thus the identified cloud belts were fragmented (Fig. 1c).
 Cloud mask results with RST are much more reasonable (Fig. 1d).

For cloud detection over sun-glint regions, SG_DLS assumes that sea surface reflectance is greater
 than that of clouds. Thus, the 3.9- μm BTs over cloudy areas should be lower than those of model
 170 simulations under clear-sky conditions. SG_DLS also estimates the contribution of the reflected sunlight

to an observed radiance by using the formula $\frac{(O_{3.9\mu m} - O_{10.4\mu m})}{O_{0.64\mu m}}$ and marks those pixels with limited
 contribution of the reflected sunlight as cloudy. During nighttime, the low-level clouds and clear-sky
 desert have very similar characteristics of 3.9- μm emissivity. Relative to ULST, DZT_NLS employs two
 extra criteria ($O_{12.4\mu m} - O_{10.4\mu m} < 0$ and
 175 $(O_{10.4\mu m} - O_{3.9\mu m} + 5) / 10 - (O_{12.4\mu m} - O_{10.4\mu m} + 4) / 6 > 0.16$) so that the clear-sky desert pixels would
 not be falsely flagged as cloudy.



180 **Figure 1: (a) A false-color image (red, 0.64 μm ; green, 1.6 μm ; blue, 11.2 μm reversed) showing land in green, thick ice clouds in magenta, and low clouds in yellow, (b) solar zenith angle (unit: degree), and (c)-(d) cloud mask results (c) without and (d) with RST at 23:00 UTC on 10 April 2023.**

185 Like other cloud mask algorithms, the NJIAS algorithm also generates a four-level mask whose categories are confidently clear, probably clear, probably cloudy, and confidently cloudy. Probably clear pixels are defined as those failing the uniformity tests, and probably cloudy pixels are those located at cloud edges.

2.3.2 Newly added snow, dust, and haze mask algorithms

190 Snow mask is an important procedure implemented before cloud mask. In the NJIAS algorithm, the pixels satisfy one of following three conditions are firstly identified as snow candidates: (1) they are over oceans with surface temperature analyses being lower than 263 K, (2) the underlying surface type is

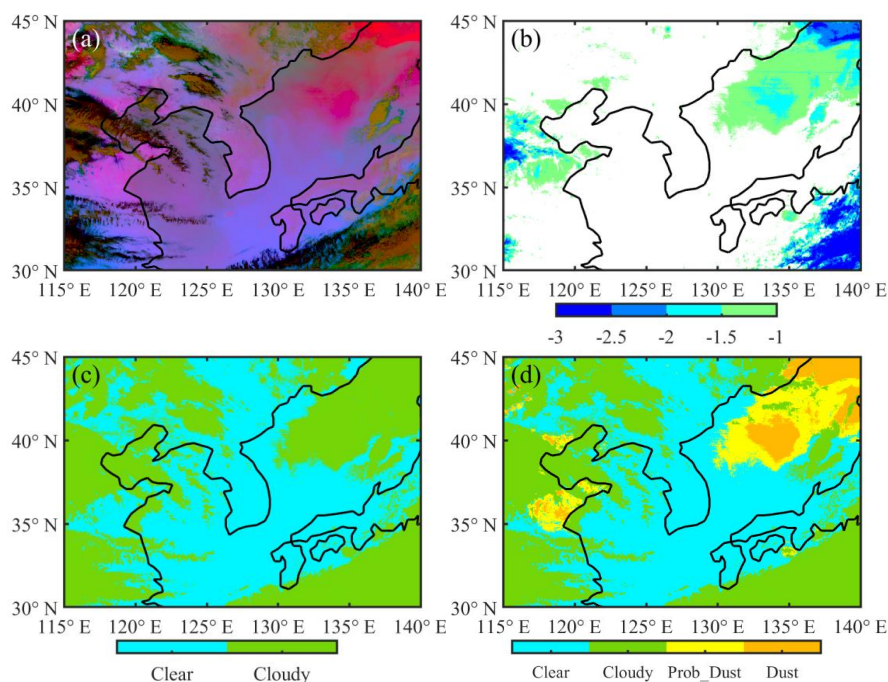
“permanent snow”, and (3) both the normalized differential snow index (NDSI; $\frac{O_{0.64\mu\text{m}} - O_{1.6\mu\text{m}}}{O_{0.64\mu\text{m}} + O_{1.6\mu\text{m}}}$) and

the enhanced NDSI ($\frac{O_{0.64\mu\text{m}}^{0.33} - O_{1.6\mu\text{m}}^{0.33}}{O_{0.64\mu\text{m}}^{0.33} + O_{1.6\mu\text{m}}^{0.33}}$) are larger than 0.1, and meanwhile the normalized differential



vegetation index $\left(\frac{O_{0.86\mu m} - O_{0.64\mu m}}{O_{0.86\mu m} + O_{0.64\mu m}} \right)$ is larger than -0.1. A series of strict tests are then performed to

195 rule out the candidates presenting unique spectral characteristics of ice clouds (e.g., mobile; visible on the water vapor images; much colder than the surface). However, the pixels that have an NDSI value greater than 0.1 and were classified as snow one hour ago would be restored to snow again.



200

Figure 2: (a) “Dust” RGB composite image (dust in pinkish color) and (b) NFMFT value (unit: K), and (c)-
 (d) cloud mask results derived from (c) old and (d) new versions of the NJIAS cloud algorithms at 09:00 UTC
 on 12 April 2023.

205

In the old version of NJIAS cloud mask algorithm, dust was often identified as cloudy, especially when it is transported over oceans. A remarkable example of this occurred at 09:00 UTC 12 April 2023 (Fig. 2). The poor performance is primarily a result of the usage of the negative channel-14 minus 15 test (NFMFT) that was originally applied to detect opaque clouds. In fact, the dust can generate a NFMFT value $\left((O_{11.2\mu m} - O_{12.4\mu m}) - (B_{11.2\mu m} - B_{12.4\mu m}) \right)$ as great as the opaque clouds, as shown in Fig. 2b.

210

Now, NFMFT is removed from the NJIAS cloud mask algorithm but added to the NJIAS dust mask



algorithm, which originally included an empirically dusk mask test developed based on the principle used by “Dust” RGB composite images (Lensky and Rosenfeld, 2008). The dusk mask is implemented after cloud mask. Accordingly, cloud mask results derived from the NJIAS cloud algorithms are improved (Fig. 2d).

215 Similar consideration is applied to haze detection. The reflectance gross contrast test (RGCT) that was employed by various cloud mask algorithms is added to the haze mask algorithm. RGCT works on the assumption that clouds have larger 0.64- μm reflectance than clear sky, which is also true for haze. The original haze mask algorithm only included a heavy aerosol test—Test 1 in Hutchison et al. (2008), assuming that haze is transparent at the 2.3- μm wavelength but much reflective at the 0.64- μm
220 wavelength.

2.3.3 Updates to the cloud-top property algorithm

The NJIAS CTH algorithm follows mainly the architecture of the ABI Cloud Height Algorithm (ACHA; Heidinger, 2012). It derives cloud-top temperature (CTT), CTH, cloud-top pressure (CTP), τ , and Re with a consistent accuracy for day and night. Note that τ and Re from the ACHA approach are
225 only reliable for cirrus clouds because the long-wave IR observations cannot provide the desired sensitivity to cloud microphysics for optically thick clouds.

The NJIAS IR cloud-top phase algorithm is developed based on Zhuge et al. (2021a). It categorizes cloudy tops into liquid-water, ice, and mixed/uncertain phases, by employing the IR-window and IR-water vapor channels as well as several spectral and spatial tests. The liquid-water phase is further refined
230 into being either supercooled-water or warm-water, depending on whether the CTT is below 0 °C or not. For ice-phase cloud tops, they are further divided into opaque-ice, cirrus, overlapped, and overshooting tops based on the results of the BT-based cirrus test, a beta-parameter-based overlap test, and a cloud-emissivity-based overshooting test (Platnick et al., 2019). In addition, a new cloud type named “broken” is defined for cirrus pixels which are located at cloud edges (i.e., cloud-mask value equals 2).

235 A pixel will be identified as probably foggy if it is liquid-water phase and the spatial uniformity (i.e., the standard deviation of 11.2- μm BTs) over a 3 \times 3 pixels array is below 0.5 K. Meanwhile, the 11.2- μm BT difference between satellite observations and model simulations should be greater than -10 (-15) K over land during daytime (nighttime) or -6 K over oceans all day. Subsequently, confidently foggy pixels are determined from the probably foggy ones if they have been classified as confidently cloudy



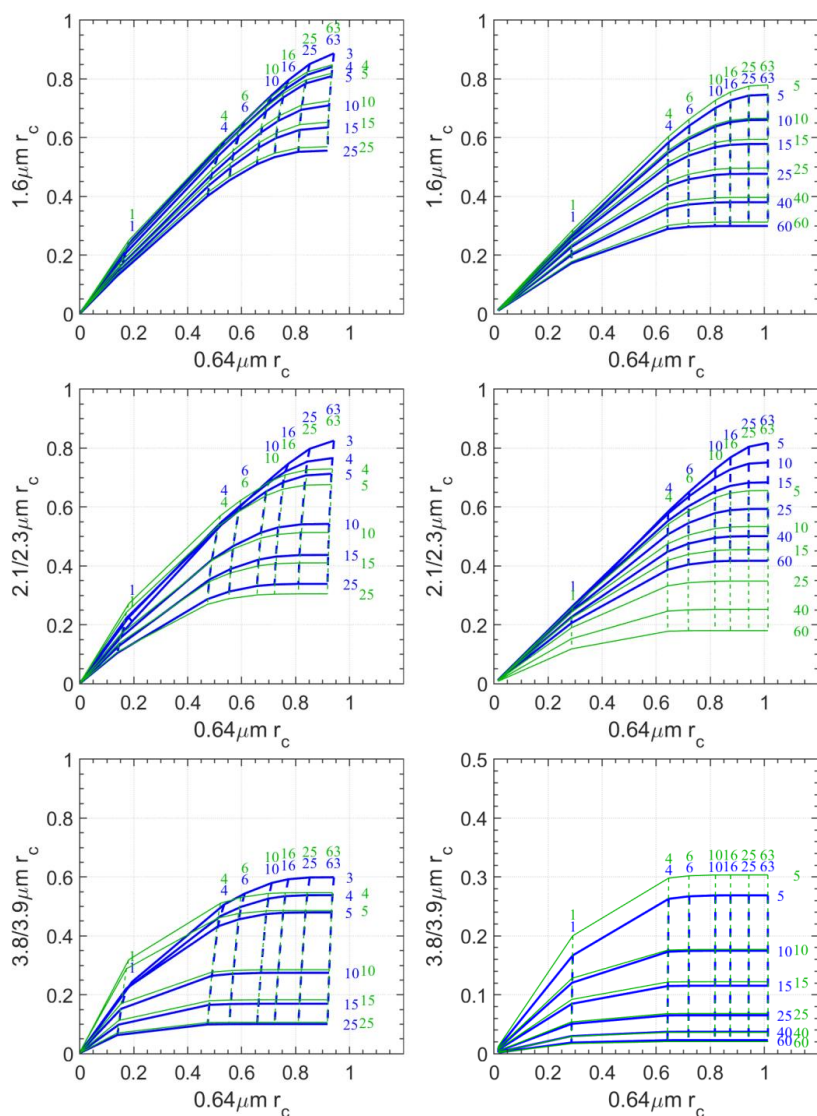
240 and their spatial uniformity are below 0.3 K.

2.3.4 Updates to the DCOMP algorithm

245 Same as Zhuge et al. (2021b), the NJIAS DCOMP algorithm uses the bispectral method described by Nakajima and King (1990) in the daytime τ and Re retrievals. Three pairs of non-absorption and water-absorption channels at visible, SWIR, and mid-wave IR wavelengths are employed to separately derive three DCOMP products (designated as DCOMP35, DCOMP36 and DCOMP37, meaning a combination of 0.64- μm and either 1.6-, 2.3-, or 3.9- μm channels, respectively). The NJIAS DCOMP algorithm utilizes parameterization schemes and retrieval procedures that are nearly consistent to those used in Zhuge et al. (2021b) except for the lookup tables (LUTs).

250 **Table 3: Grid point values of the LUT parameters.**

Parameter	Number of points	Grid point values
Re (μm)	16	3, 4, 5, 6, 7, 8, 9, 10, 12, 14, 16, 18, 20, 22, 24, 25 (liquid-water cloud)
	12	5, 10, 15, 20, 25, 30, 35, 40, 45, 50, 55, 60 (ice cloud)
τ	34	0.05, 0.10, 0.25, 0.5, 0.75, 1.0, 1.25, 1.5, 1.75, 2.0, 2.39, 2.87, 3.45, 4.14, 4.97, 6.0, 7.15, 8.58, 10.30, 12.36, 14.83, 17.80, 21.36, 25.63, 30.76, 36.91, 44.30, 53.16, 63.80, 76.56, 91.88, 110.26, 132.31, 158.78
μ_{sat}	28	0.40, 0.45, 0.50, 0.55, 0.60, 0.65, 0.70, 0.75, 0.7625, 0.7750, 0.7875, 0.8000, 0.8125, 0.8250, 0.8375, 0.8500, 0.8625, 0.8750, 0.8875, 0.900, 0.9125, 0.9250, 0.9375, 0.9500, 0.9625, 0.9750, 0.9875, 1.0
μ_{sol}	33	0.15, 0.20, 0.25, 0.30, 0.35, 0.40, 0.45, 0.50, 0.55, 0.60, 0.65, 0.70, 0.75, 0.7625, 0.7750, 0.7875, 0.8000, 0.8125, 0.8250, 0.8375, 0.8500, 0.8625, 0.8750, 0.8875, 0.900, 0.9125, 0.9250, 0.9375, 0.9500, 0.9625, 0.9750, 0.9875, 1.0
$\Delta\varphi$ ($^\circ$)	37	0:5:180



255

Figure 3: Variations of r_c at $0.64 \mu\text{m}$ and either 1.6 (top panels), ~ 2.2 (middle panels), or $\sim 3.8 \mu\text{m}$ (bottom panels) for $Re = 3, 4, 5, 10, 15$ and $25 \mu\text{m}$ (solid curve) and $\tau = 1, 4, 6, 10, 16, 25$ and 63 (dashed curve) for liquid-water phase (left panels) and for $Re = 5, 10, 15, 25, 40$ and $60 \mu\text{m}$ (solid curve) and $\tau = 1, 4, 6, 10, 16, 25$ and 63 (dashed curve) for ice phase (right panels) from Collection-6.1 MYD06 (green) and NIAS (blue) datasets when $\mu_{\text{sol}} = \mu_{\text{sat}} = 0.5$ and $\Delta\phi = 60^\circ$.

260

Forward radiative transfer calculations for the LUTs were performed with the discrete ordinates



radiative transfer (DISORT) model implemented in libRadTran 2.0.3 (Mayer and Kylling, 2005; Emde et al., 2016). The atmospheric temperature and humidity profile is the U.S. Standard Atmosphere, and
265 the absorption /scattering by air molecules or aerosols are neglected. The cloud layer is assumed to be 1 km thick and placed at an altitude of 5 km above a non-reflecting surface. The bulk single-scattering properties of clouds are considered separately for liquid-water and ice clouds. For liquid-water clouds, the scattering properties of water droplets are computed from Lorenz–Mie theory, assuming a gamma size distribution. For ice clouds, a scattering parameterization named Baum_v36 (Heymsfield et al., 2013;
270 Yang et al., 2013; Baum et al., 2014) with ice crystal habit of severely roughened aggregated column is used. The water droplet and ice crystal assumptions are identical to those in the Collection-6.1 MYD06 algorithm. The final LUTs of cloud emissivity, reflectance, and transmissions as well as the spherical albedo are functions of R_e , τ , the cosine of satellite zenith angle (μ_{sat}), the cosine of solar zenith angle (μ_{sol}), and the relative azimuth angle ($\Delta\varphi$). Table 3 summarizes the grid point values for R_e , τ , μ_{sat} ,
275 μ_{sol} and $\Delta\varphi$ used in constructing the LUTs. Figure 3 shows visualizations of cloud reflectance (r_c) at 0.64 μm and either 1.6, \sim 2.2, or \sim 3.8 μm for liquid-water and ice clouds for an arbitrarily chosen solar-viewing geometry. Green and blue curves are the LUTs used by Collection-6.1 MYD06 and NIAS algorithms, respectively. Relative to the pairs of 0.64–1.6- μm channels and 0.64– \sim 3.8- μm channels, the pair of 0.64– \sim 2.2- μm channels has a noticeable difference in the LUTs of r_c between MYD06 and
280 NIAS algorithms. The 2.3- μm r_c values of the NIAS LUTs are systematically larger than the 2.1- μm r_c values of the MYD06 LUTs when the τ , R_e , and solar-viewing geometry are same. This characteristic is especially significant for ice clouds.

Once τ and R_e are determined, these two retrievals are used subsequently to calculate the total mass of water in a cloud column, known as liquid water path (LWP) and ice water path (IWP) for liquid-water and ice clouds, respectively. Assuming a vertical homogeneity of cloud, LWP (IWP) is derived using
285

$$\frac{4\rho}{3Q_e} R_e \tau \quad (\text{Stephens, 1978; Khanal and Wang, 2018}),$$
 where ρ is the density of liquid water (ice),

and Q_e is the liquid water (ice) extinction efficiency. Meanwhile, the CTP and τ retrievals are applied for determining cloud types based on the International Satellite Cloud Climatology Project (ISCCP) rule



(Rossow and Schiffer, 1999).

290 2.4 Cloud products

Currently, the NJIAS HCFD has two cloud products, namely 0.04Deg (on regular latitude-longitude grids at $0.04^\circ \times 0.04^\circ$ resolution) and TyWNP (for WNP Typhoons). The 0.04Deg and TyWNP products can be directly derived from the full-disk measurements by a projection transformation. For the TyWNP product, typhoon center positions are determined by the tropical-cyclone-red-green-blue (TC-RGB) composites, as introduced in Chen et al. (2022). Table 4 lists the coverage in space and time for two products. Users can select any of the two cloud products appropriate for their purpose.

Table 4: Brief descriptions of two products of the NJIAS HCFD.

Product Name	Variables Included	Domain Coverage	Time Period	Spatial Resolution	Time Interval
0.04Deg	all variables except ShadowMask, HazeMask, FireMask, SST	$50^\circ \text{N} - 10^\circ \text{N}$, $90^\circ \text{E} - 170^\circ \text{W}$	April 2016–December 2022	0.04°	30 minutes
TyWNP	all variables except ShadowMask, SnowMask, DustMask, HazeMask, FireMask, SST	a $20^\circ \times 20^\circ$ longitude-latitude grid box surrounding the typhoon center	typhoon seasons from 2016 to 2022	0.02°	

300 3 Evaluation of the NJIAS HCFD

In this section, results obtained by the NJIAS cloud mask and cloud-top phase algorithms are objectively evaluated at the pixel level against the CALIOP 1-km cloud layer products of version 4.20 (Avery et al., 2020) in the whole year of 2017. Because the CALIOP and AHI operate under different sampling schemes, only those AHI pixels within which the CALIOP cloud identification results are in complete agreement are retained. The temporal difference between CALIOP and AHI observations is limited to ± 15 min. Also evaluated against CALIOP data are the Collection-6.1 MYD06 and JAXA cloud products to make a comparison on the performance of NJIAS HCFD with these two existing cloud feature datasets.

Collection-6.1 MYD06 dataset is employed to evaluate the NJIAS cloud height and DCOMP



310 retrievals. Similar to the collocation between CALIOP and AHI pixels, all of the MODIS pixels within
 one AHI pixel shall have a consistent phase, otherwise this MODIS-AHI data pair will not be included.
 For those pairs that are retained, the retrievals of MODIS pixels within each matched AHI pixel are
 averaged first before the comparison with the AHI retrievals.

3.1 Cloud mask results

315 The CALIOP columns with zero cloud layer are assigned to clear-sky category, and those with at
 least one cloud layer are assigned to cloudy category. Figure 4 shows the percentages of confidently clear,
 probably clear, probably cloudy and confidently cloudy pixels in MYD06, NJIAS and JAXA cloud-mask
 results for CALIOP cloudy and clear-sky pixels. It is noted that the JAXA product has the largest
 proportions of probably cloudy and the smallest proportions of probably clear pixels among three cloud
 320 products. Overall, the MYD06 classifications are in best agreement with those of CALIOP with higher
 confidence during daytime. The NJIAS classification results are similar to the MODIS results with
 fractional differences of less than 10%.

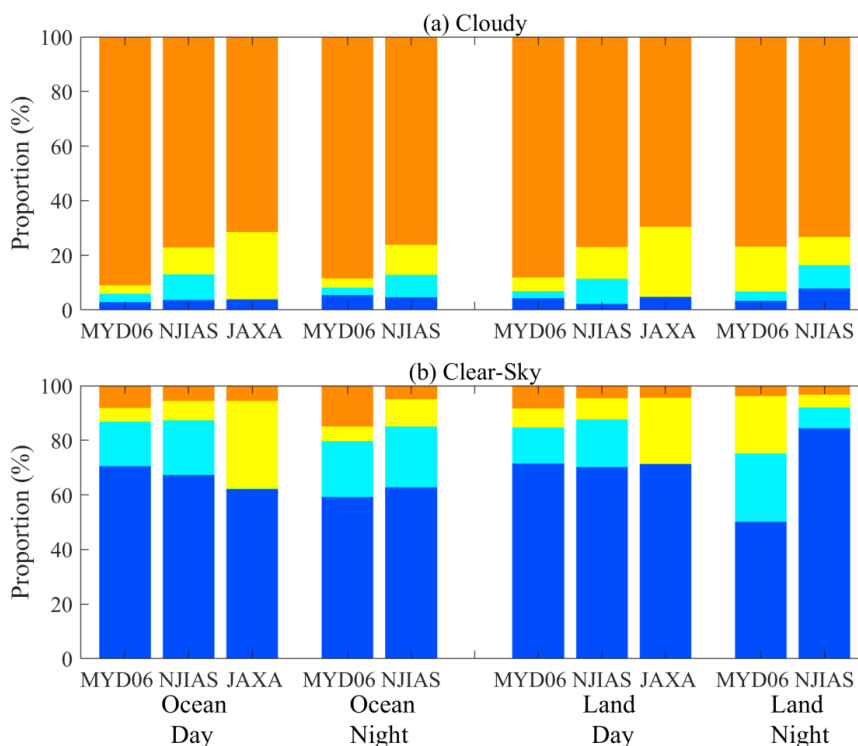




Figure 4: Proportions of confidently clear (blue), probably clear (cyan), probably cloudy (yellow), and confidently cloudy (orange) pixels in MYD06, NJIAS and JAXA cloud-mask results for CALIOP-observed (a) cloudy and (b) clear-sky pixels in 2017.

To quantitatively evaluate the cloud-mask retrievals, the following four indices are introduced: probability of detection (POD), false-alarm rate (FAR), Heike skill score (HSS), and the equitable threat score (ETS). The definitions of the POD, FAR, HSS and ETS were described in Zhuge et al. (2011). Table 5 lists the scores of POD, FAR, HSS and ETS for cloud-mask retrievals of three datasets. Here, confidently cloudy and probably cloudy are grouped as “cloudy” while confidently clear and probably clear are grouped as “clear”. It can be seen that MYD06 and JAXA datasets always have a POD greater than 90%, regardless over oceans or land. The MYD06 also has a low FAR for all scenarios except during nighttime over land. In contrast, the JAXA dataset has high FARs of more than 13% over oceans and land. The PODs and FARs for the NJIAS algorithm are ~85% and ~6%, respectively. Consequently, the NJIAS HCFD achieves an HSS of 0.73 and an ETS of 0.58 during nighttime over land, surpassing the MYD06 dataset which has an HSS of 0.70 and an ETS of 0.54. In other scenarios, the NJIAS HCFD lags behind the MYD06, but outperforms the JAXA dataset.

340

Table 5: Sample sizes and POD, FAR, HSS and ETS scores for cloud-mask retrievals of MYD06, NJIAS and JAXA datasets over oceans and land and during daytime and nighttime when validated with CALIOP products in the whole year of 2017.

		Sample Size	POD	FAR	HSS	ETS
Ocean Day	MYD06	1356513	93.98%	6.72%	0.8118	0.6833
	NJIAS	1356513	86.78%	6.94%	0.7202	0.5628
	JAXA	1356513	95.95%	16.85%	0.6292	0.4590
Ocean Night	MYD06	1247314	91.73%	8.05%	0.7145	0.5558
	NJIAS	1247314	87.03%	6.36%	0.6855	0.5215
Land Day	MYD06	359061	92.94%	8.01%	0.7816	0.6416
	NJIAS	359061	88.48%	6.85%	0.7468	0.5959
	JAXA	359061	95.02%	13.80%	0.6967	0.5346
Land Night	MYD06	483911	93.10%	14.47%	0.7024	0.5413
	NJIAS	483911	83.42%	5.62%	0.7327	0.5781



345 **3.2 Cloud height results**

Since there is an intrinsic difference in the cloud tops between lidar measurements versus IR estimates, the NJIAS cloud height retrievals are evaluated against the MYD06 instead of the CALIOP CTH products. Figure 5 shows the joint probability histograms of three cloud height parameters (CTT, CTH and CTP) between the MYD06 and NJIAS datasets in June and December 2017. Overall, the NJIAS cloud height parameters agree well with the MYD06 retrievals. The correlation coefficient (CC) is greater than 0.9. The multiplicative biases (MBs) are between 0.98 and 1.02, indicating no noteworthy underestimation or overestimation. The root-mean-square errors (RMSE) for CTT, CTH and CTP are 12.9 K, 2.0 km and 112 hPa, respectively.

355

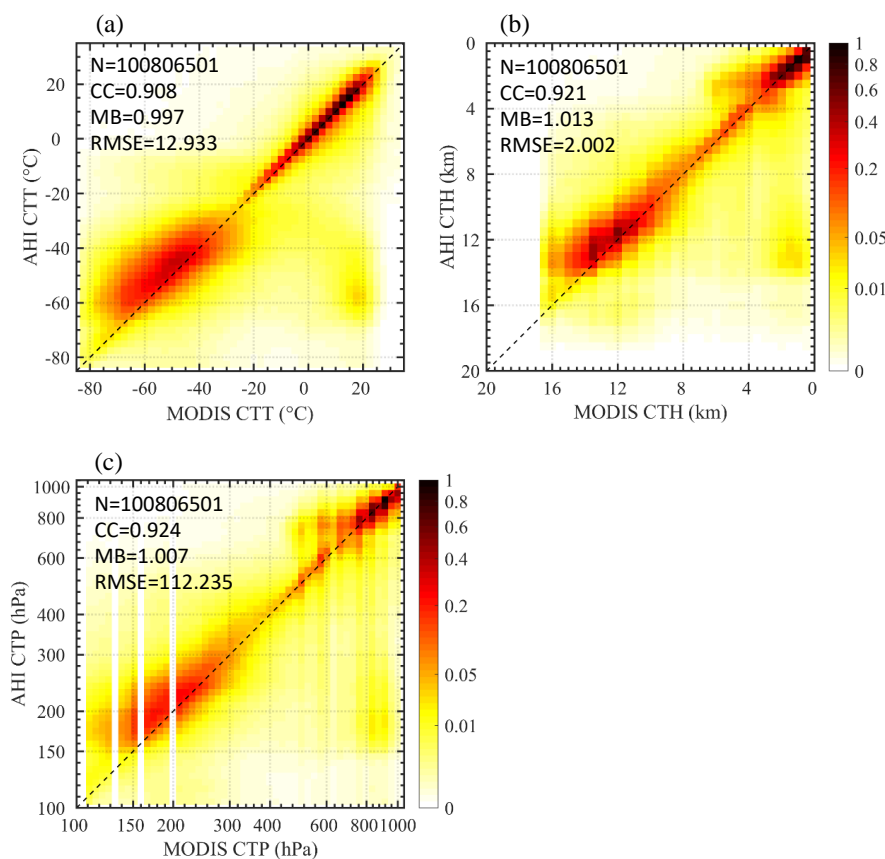


Figure 5: Joint probability density histograms of (a) CTT, (b) CTH, and (c) CTP between MYD06 and NJIAS datasets in June and December 2017. Also indicated in each panel are sample size (N), correlation coefficient

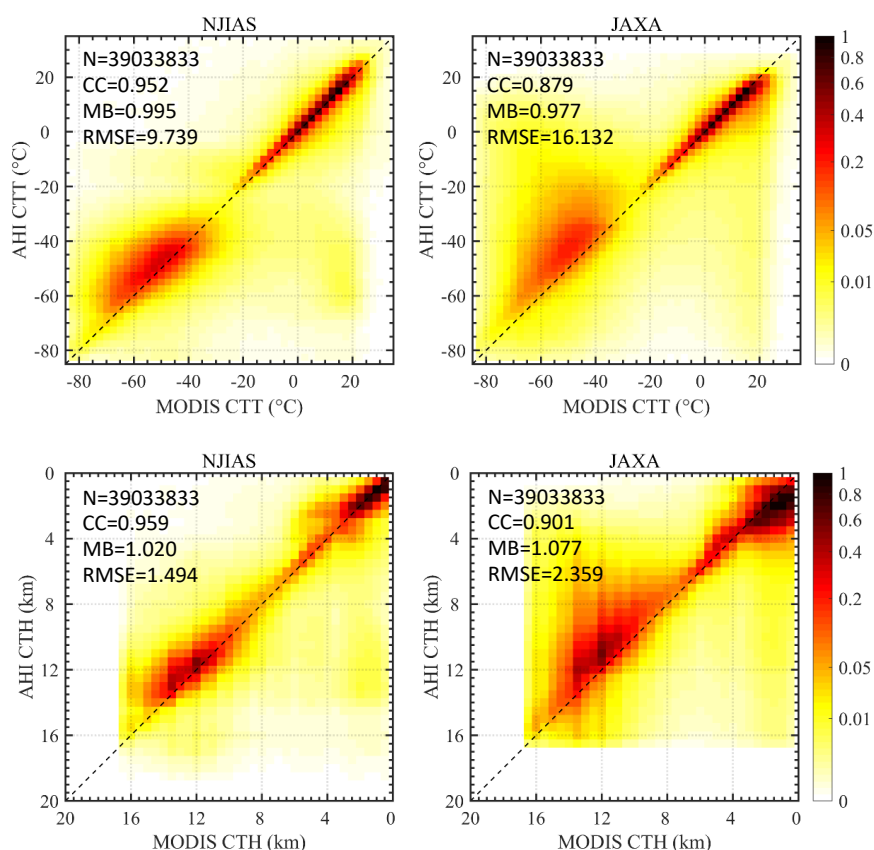


(CC), multiplicative bias (MB) and root-mean-square error (RMSE).

360

The JAXA dataset includes two cloud height parameters CTT and CTH, which are available only in daytime. By comparing NJIAS daytime CTT and CTH retrievals to JAXA's results, Figure 6 confirms the remarkable improvement in the accuracy of these two cloud height parameters yielded by the NJIAS. The JAXA retrievals exhibit a tendency to overestimate the CTT and underestimate the CTH of mid-to-high-level clouds. As a result, the RMSE values for the JAXA CTT and CTH retrievals are 16.1 K and 2.4 km, respectively, which are much larger than the metrics of 9.7 hPa and 1.5 km for the NJIAS retrievals.

365



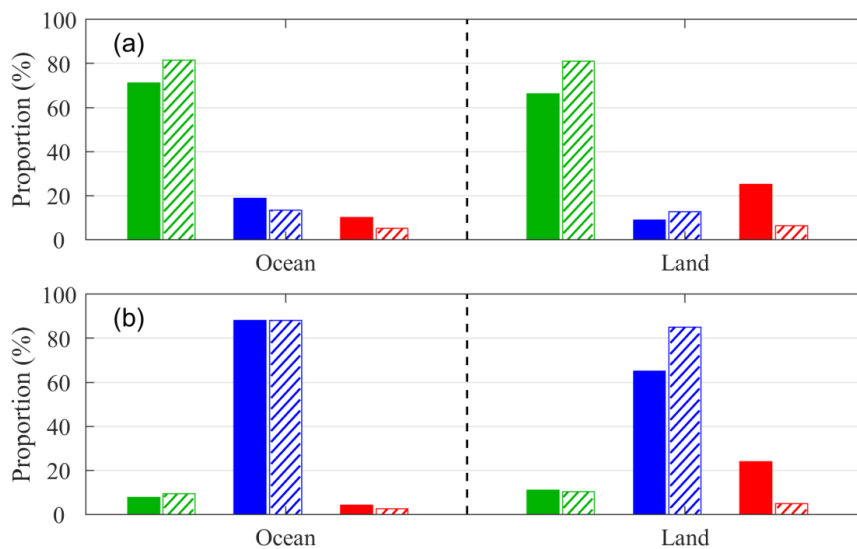
370

Figure 6: Joint probability density histograms of CTT (top panels) and CTH (bottom panels) between MYD06 and NJIAS (left panels) and between MYD06 and JAXA (right panels) datasets in daytimes of June and December 2017.



375 3.3 Cloud-top phase results

The CALIOP cloud-top phase is defined as the CALIOP cloud phase of the uppermost cloud layer, which will serve as the truth in the following evaluations. The CALIOP classification currently provide four categories of phases, that is, liquid-water, randomly oriented-ice (ROI), horizontally oriented-ice, and unknown (Hu et al., 2009). The latter two categories are not considered in this study because of their
380 percentages of occurrence (less than 1.0%) (Zhuge et al., 2021a). In addition, the Collection-6 MYD06 dataset provides two independent cloud-top phase retrievals. One is an IR-only results available all day, and the other is derived from a combination of SWIR and IR tests that runs during daytime only (Baum et al., 2012).



385 **Figure 7: Proportions of liquid-water (green), ice (blue), and mixed/uncertain (red) phases identified by MYD06 IR-only (solid bars) and NIAS (hatched bars) for CALIOP pixels with (a) liquid-water- and (b) ROI-phase cloud tops in 2017 over oceans and land. Clear pixels identified by either MYD06 or NIAS are excluded from the statistics.**

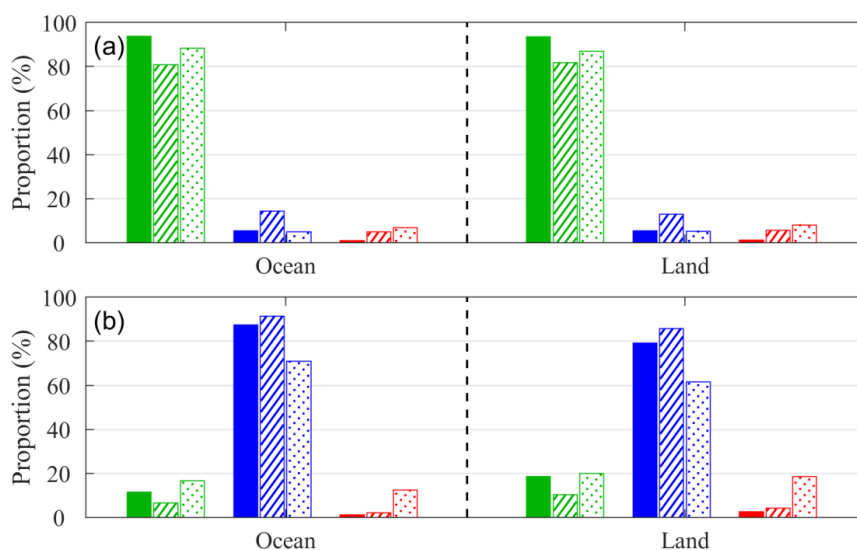
390

Figure 7 demonstrates that the NIAS cloud-top phase retrievals perform better than the MYD06 IR-only retrievals. For CALIOP liquid-water and ROI cloud tops over oceans, the PODs of NIAS



retrievals are 81.6% and 88.2%, respectively. These two metrics slightly decrease to 81.1% and 85.0% over land. Over oceans, the MYD06 IR-only and NIAS datasets exhibit similar behavior for CALIOP
 395 ROI cloud-top phases. However, compared to NIAS HCFD, the MYD06 IR-only dataset tends to classify more CALIOP liquid-water phases as ice or uncertain phases, resulting in a POD of 71.2%. Over land, the MYD06 IR-only dataset classifies many CALIOP cloud tops as having an uncertain phase, resulting in low PODs of only 66.2% and 65.1% for CALIOP liquid-water and ROI cloud tops, respectively.

400

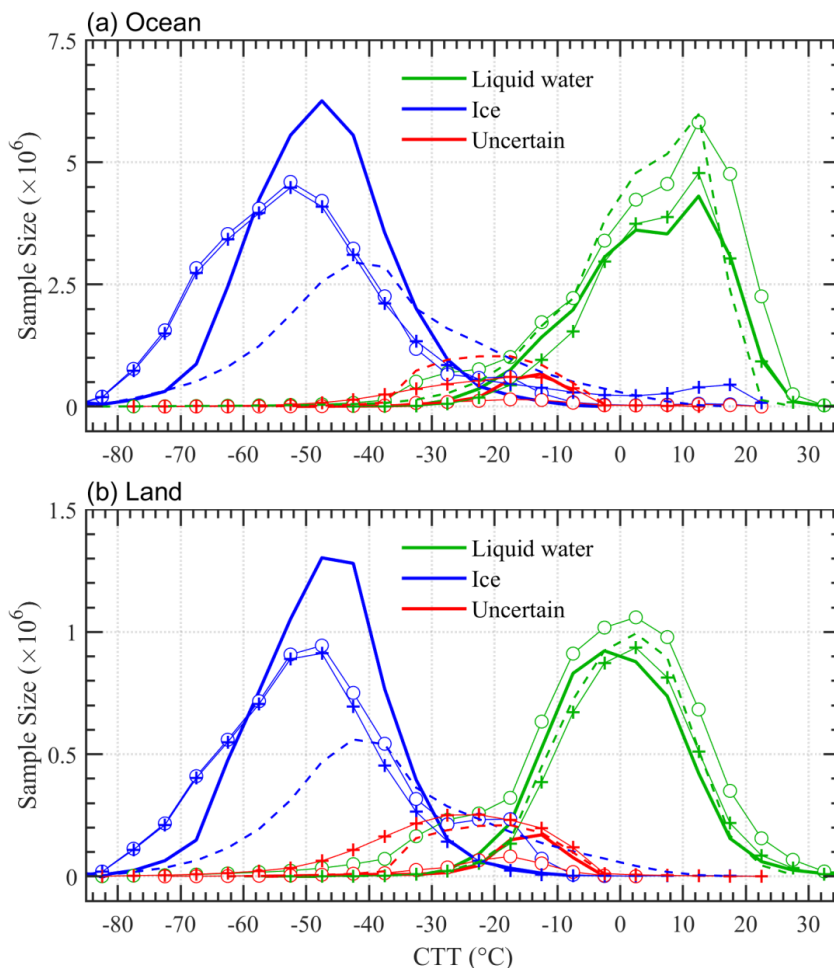


**Figure 8: Proportions of liquid-water (green), ice (blue), and mixed/uncertain (red) phases identified by MYD06 SWIR+IR (solid bars), NIAS (hatched bars) and JAXA (dotted bars) for CALIOP pixels with (a) liquid-water- and (b) ROI-phase cloud tops in daytimes of 2017 over oceans and land. Clear pixels identified
 405 by MYD06, NIAS, or JAXA are excluded from the statistics. Only daytime data are retained.**

Intercomparisons of cloud-top phase retrievals are also made among the MYD06 SWIR+IR, the NIAS, and the JAXA datasets during daytime only (Fig. 8). It can be seen that NIAS cloud-top phase retrievals exhibit a consistent accuracy for both day and night. Meanwhile, the MYD06 SWIR+IR
 410 retrievals (Fig. 8) show a significant improvement over the IR-only retrievals (Fig. 7) by supplementing the IR tests with those from solar channels. Figure 8 also reveals a deficiency of the JAXA retrievals in identifying ice phases. The PODs of the JAXA dataset for CALIOP ROI phases are as low as 71.0% over



oceans and 61.5% over land, which are significantly worse than those for CALIOP liquid-water phases.



415

Figure 9: Sample size variations of cloud-top phases identified by MYD06 IR-only (plus signs connected by thin lines), MYD06 SWIR+IR (open circles connected by thin lines), NJIAS (thick solid curves) and JAXA (dashed curves) with respect to the CTT values in daytimes of June and December 2017 over (a) oceans and (b) land.

420

It is worthwhile to examine the distributions of the MYD06 IR-only, MYD06 SWIR+IR, NJIAS and JAXA identified cloud-top phases with respect to the CTT values (Fig. 9). The NJIAS HCFD tends to classify cloudy pixels with CTT above 0°C as liquid-water and those with CTT below -30°C as ice.

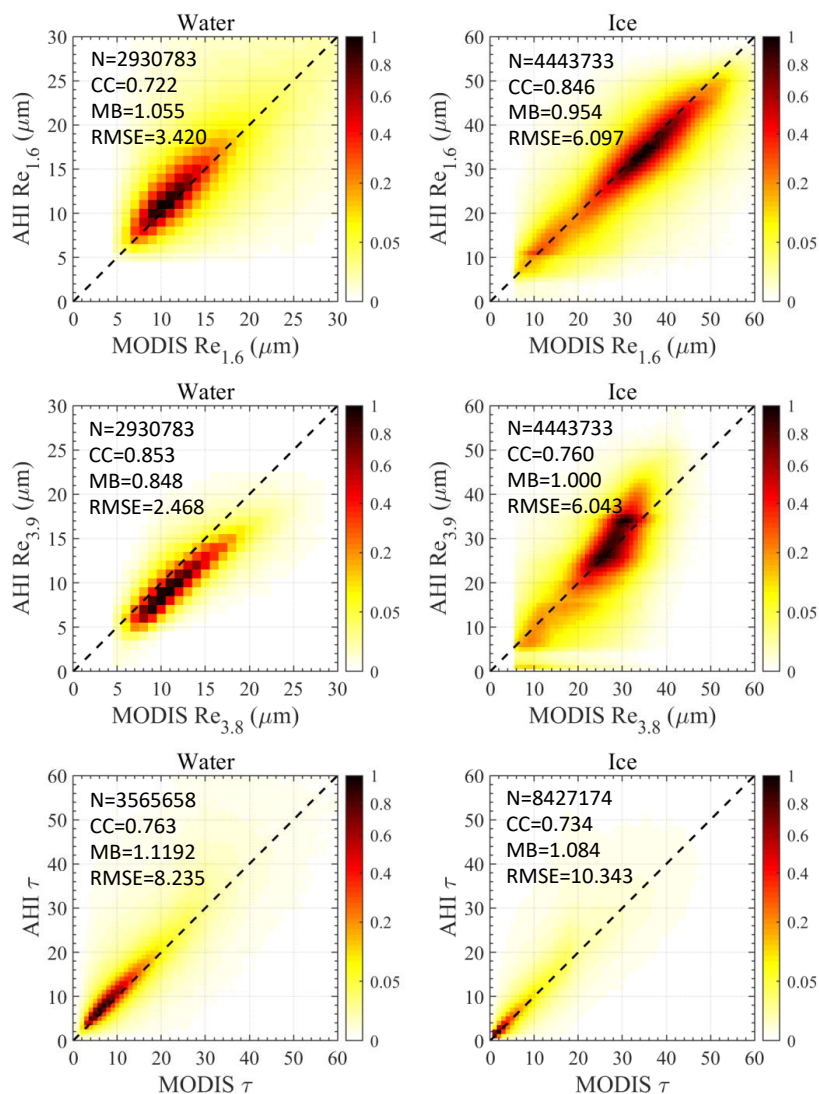


When CTT is between -30°C and 0°C , the NJIAS-identified cloud-top phase could be liquid water, ice,
425 or a mixture of both. However, there are cases where the MYD06 IR-only or the JAXA classified cloud
tops with a CTT greater than 0°C as ice phase, revealing a limitation of these two products. Continent
cloud tops with uncertain (liquid-water) phase are also found in the MYD06 IR-only (SWIR+IR)
retrievals when CTT is below -40°C . Considering that in situ observations have not revealed the presence
of a mixed or supercooled-water phase at temperatures below -40°C (Korolev et al., 2017), it is necessary
430 to reexamine the two MYD06 cloud-top phase classifications over land.

3.4 DCOMP results

The NJIAS DCOMP retrievals are evaluated using the Collection-6.1 MYD06 products in June,
July and August 2017. Note that both the NJIAS and the MYD06 have three τ retrievals. In most cases
these three τ retrievals are nearly identical. Accordingly, the DCOMP35 τ is selected as a representative
435 in this study. Besides, since all current bispectral-based DCOMP algorithms have large uncertainties or
errors in the Re retrievals of thin clouds, samples with τ less than 5 are removed during the Re evaluations.

Figure 10 illustrates pixel-to-pixel comparisons of Re and τ between the MYD06 and NJIAS
retrievals. The NJIAS $\text{Re}_{1.6}$ retrievals are generally consistent with the MYD06 $\text{Re}_{1.6}$ values for both
liquid-water and ice clouds. Most samples are distributed evenly around the one-to-one ratio lines. The
440 CC of the NJIAS $\text{Re}_{1.6}$ retrievals for liquid-water (ice) clouds is 0.72 (0.85), and the corresponding MB
and RMSE values are 1.06 (0.95) and $3.42\mu\text{m}$ ($6.10\mu\text{m}$), respectively. The NJIAS $\text{Re}_{3.9}$ retrievals for
liquid water clouds are systematically smaller than their MYD06 counterparts that has an MB of 0.85
and a CC of 0.85. However, such an underestimation is not found in the NJIAS $\text{Re}_{3.9}$ retrievals for ice
clouds, which yielded an MB of 1.00, a CC of 0.76 and a RMSE of $6.04\mu\text{m}$. Overall, the NJIAS τ
445 retrievals agree well with the MYD06 τ values for both liquid-water and ice clouds. The MB ranges from
1.08 to 1.12, and the CC ranges from 0.73 to 0.76.



450

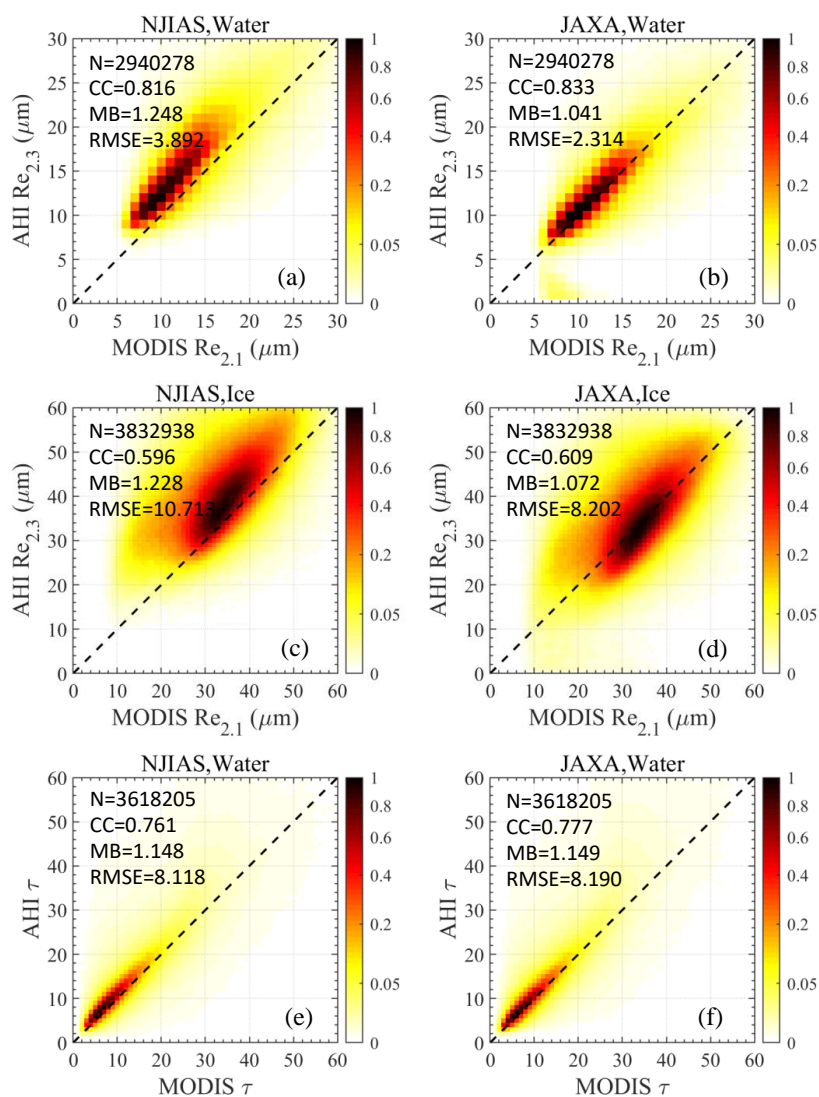
Figure 10: Joint probability density histograms of $Re_{1.6}$ (top panels), $Re_{3.8}$ [$Re_{3.9}$] (middle panels), and τ (bottom panels) between MYD06 and NIAS datasets for liquid water (left panels) and ice (right panels) clouds in daytimes of June, July and August 2017.

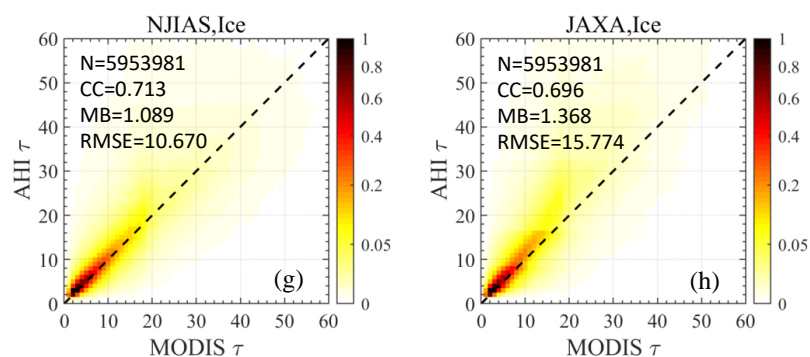
455

The JAXA dataset only provides one pair of Re and τ derived using 0.64- μm and 2.3- μm channels. Figure 11 compares the results between the NIAS and JAXA retrievals. Note that the sample sizes are less than those in Fig. 10 due to a large amount of retrieval failures in the JAXA algorithm. The NIAS



460 $Re_{2,3}$ retrievals in both liquid-water and ice clouds show a systematic overestimation ($\sim 2 \mu\text{m}$) when MYD06 $Re_{2,1}$ retrievals are regarded as the “truth”. The overestimations are likely due to a discrepancy in the sensor central wavelengths which will affect the reflectance observations and the DCOMP LUTs (Wang et al., 2018). Interestingly, the overestimations are not found in the JAXA retrievals. A detailed comparison of the LUTs used by the NJIAS and the JAXA is essential. The performances of τ retrievals from NJIAS and JAXA are similar in general, except for a slight overestimation of ice clouds in the 465 JAXA products.





470

Figure 11: Joint probability density histograms of (a–d) $Re_{2.1}$ [$Re_{2.3}$] and (e–h) τ between MYD06 and NJIAS (left panels) and between MYD06 and JAXA (right panels) datasets for (a–b, e–f) liquid-water and (c–d, g–h) ice clouds in daytimes of June, July and August 2017.

4 Application Examples

475 4.1 Cloud climatology in southwestern China

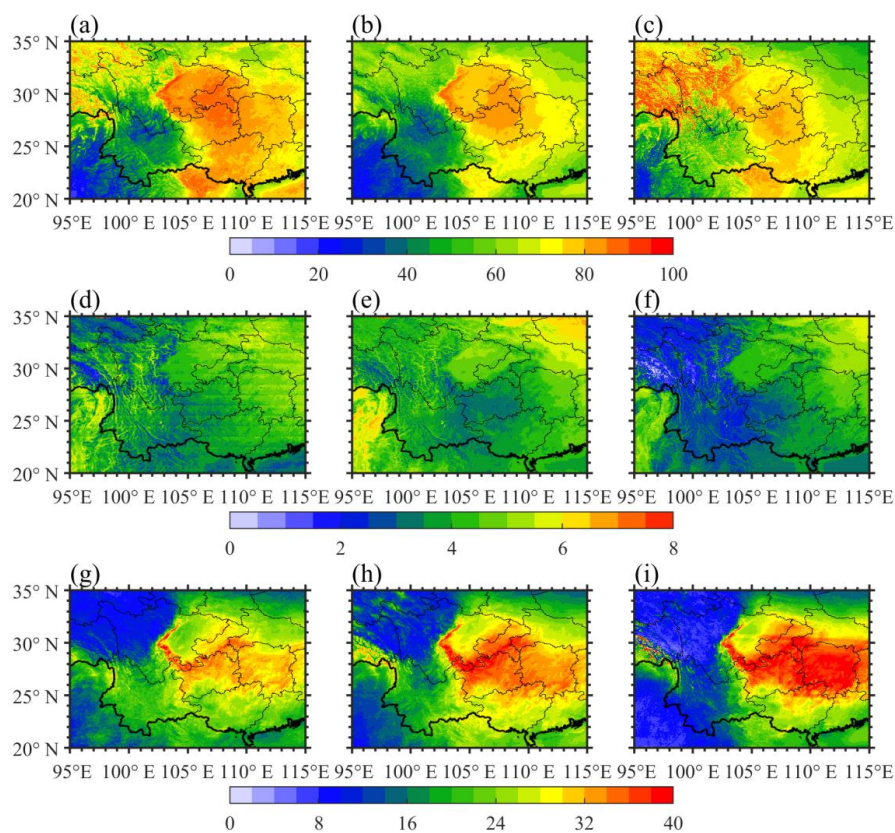
The climate in southwestern China is controlled by the East Asian and South Asian monsoons, in combination with the complex terrain. During the cold season (November–April), a quasi-stationary front frequently occurs over the Yunnan–Guizhou Plateau (Cai et al., 2022), resulting in a sharp contrast of weather conditions on its two sides: cloudy or rainy sky in Guizhou province (103° – 109° E, 24° – 29° N) but clear sky in Yunnan province (97° – 106° E, 21° – 29° N). Meanwhile, the moist environment and calm winds provide favorable conditions for the frequent foggy weather over the Sichuan Basin (103° – 108° E, 28° – 32° N).

Figure 12 presents a simple analysis of the cloud climatology over southwestern China based on the cloud products in the cold seasons of years 2016–2020. Three daytime variables including cloud mask, CTH and τ are employed. The MODIS/Aqua provides daytime observations at most once per day, at $\sim 13:30$ local solar time. Therefore, results from the MYD06 are for reference only. It can be seen that the NJIAS HCFD provides a reasonable description of the spatial distribution of cloud covers over southwestern China in the cold season. The cloud occurrence frequencies are $\sim 30\%$ over Yunnan and $\sim 80\%$ over Guizhou. However, the JAXA dataset presents a weaker contrast of cloud occurrence frequencies on the two sides of the quasi-stationary front. The cloud occurrence frequencies are as high as $\sim 50\%$ over Yunnan, which is only 30% less than those over Guizhou. Moreover, the JAXA returns a

490



factitious high-frequency of greater than 90% of cloud occurrences in the eastern part of the Tibetan Plateau (95°–103° E, 26°–35° N), which is likely a result from mislabeling glacier or snow-covered areas as clouds (figures omitted). The spatial distributions of averaged CTH also exhibit large differences
495 between the NJIAS and JAXA datasets. The JAXA tends to underestimate the CTH, especially in the areas where cloud covers are obviously overestimated. For the spatial pattern of the averaged τ , there is a distinct regional difference between the eastern and western parts of southwestern China. Thick clouds often occur over the eastern part of southwestern China while thin clouds often occur over the western part, which are revealed by both the NJIAS and JAXA datasets. Nonetheless, the thick (thin) clouds tend
500 to have a greater (smaller) τ in the JAXA dataset than those in NJIAS dataset.



505 **Figure 12:** Spatial distributions of (a–c) cloud occurrence frequency (unit: %), (d–f) averaged CTH (unit: km AGL) and (g–i) τ (unitless) within $0.05^\circ \times 0.05^\circ$ grid boxes over southwestern China using 5-yr boreal cold-season cloud products of MYD06 (left panels), NJIAS (center panels), and JAXA (right panels). Only daytime data are retained.



510 4.2 Cloud and precipitation features of landfalling typhoons

The NJIAS HCFD–TyWNP provides a comprehensive description of cloud macro- and micro-physical characteristics within a $20^\circ \times 20^\circ$ longitude-latitude grid box surrounding the center of WNP typhoons. This product is useful for understanding cloud and precipitation features of typhoons. Figure 13 illustrates the utility of NJIAS HCFD–TyWNP for analyzing the intensity of typhoon rainfall in In-Fa (2021) and Hagupit (2020). The typhoon In-Fa (202106) made its first landfall at 04:30 UTC on 25 July 2021 on Zhoushan Islands at the northern coast of Zhejiang Province, with a minimum central pressure of 970 hPa according to the best-track records (Lu et al., 2021). Prior to its first landfall in Zhejiang, the central dense overcast (CDO) of In-Fa gradually disintegrated and the convection weakened. The eastern half of CDO was characterized by extensive cumulonimbus clouds with a CTH of 14 km. Due to land effects, the western half of CDO was dominated by liquid-water clouds, with a significantly low CTH and very weak vertical motion. As a result, within 24 hours before and after In-Fa made the first landfall, most areas of Zhejiang province experienced a stable stratiform precipitation. The rain rates measured by rain gauges were generally weak, mainly 5–20 mm h⁻¹, and the local maximum rain rate was only 49.0 mm h⁻¹. The rain rate at the landing site was only 29 mm h⁻¹. In contrast, typhoon Hagupit (202004) made its landfall at 19:30 UTC on 3 August 2020 in southeastern Zhejiang, with a minimum central pressure of 965 hPa, similar to the intensity of Infa (202106) making landfall.. However, during the landfall of Hagupit, the CDO distribution was complete and compact. As a result, rainstorms were produced along the track of Hagupit. The maximum rain rate measured by rain gauges in Zhejiang during the 24 hours before and after Hagupit’s landfalling time was 98.7 mm h⁻¹.

530

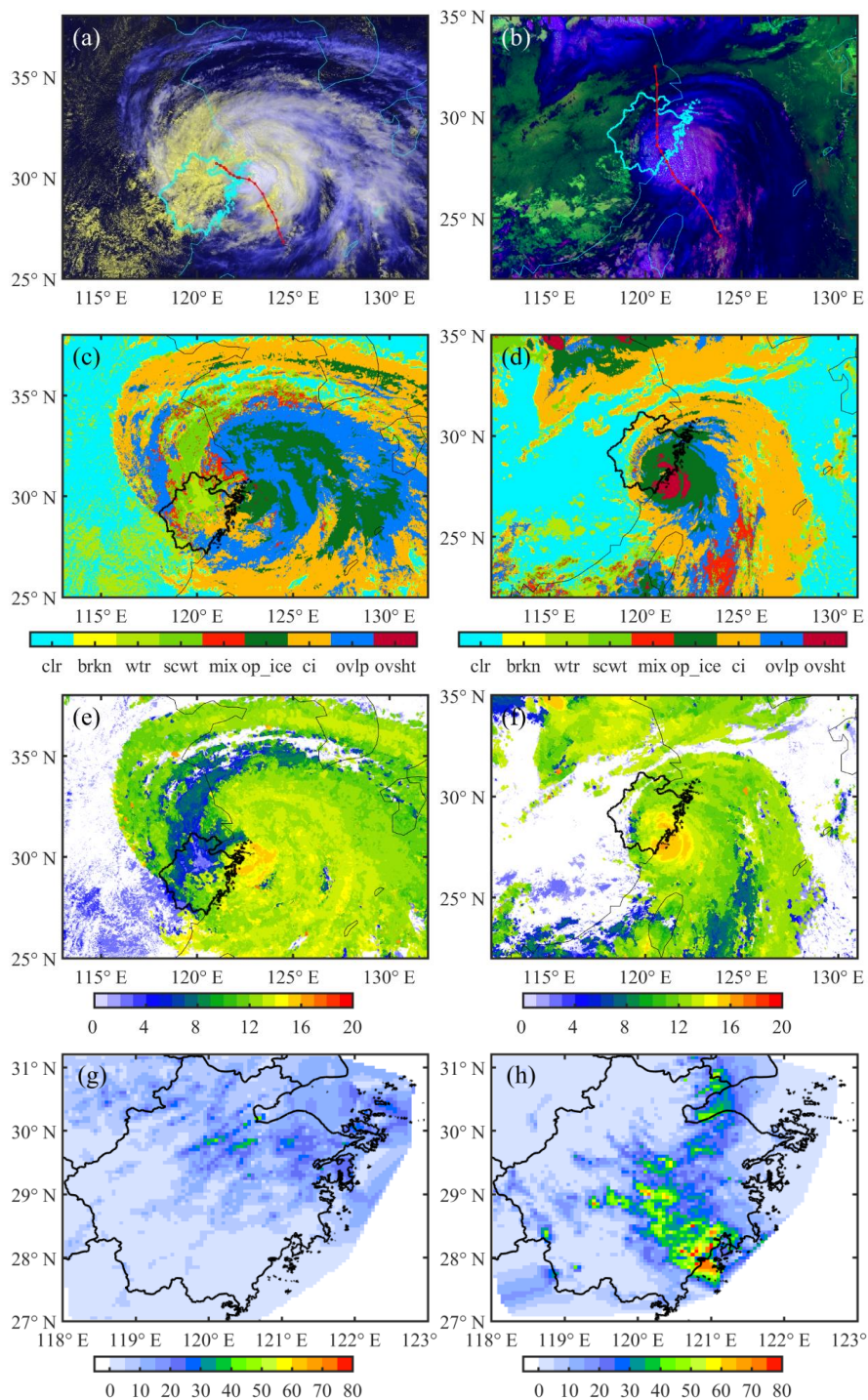




Figure 13: (a–b) TC-RGB composite images introduced in Chen et al. (2022), (c–d) cloud types including clear (clr), broken (brkn), warm-water (wtr), supercooled-water (scwt), mixed (mix), opaque-ice (op_ice), cirrus (ci), overlapped (ovlp), and overshooting (ovsht), and (e–f) CTH (unit: km AGL) at the landfalling time t_{lf} , as well as (g–h) maximum rain rate within the $t_{lf} \pm 24$ h time window (unit: mm h^{-1}) for Typhoons In-Fa (202106) (left panels) and Hagupit (202004) (right panels). The thick lines denote the boundaries of Zhejiang province. The red curve denotes the typhoon track at 3-h interval during the $t_{lf} \pm 24$ h time window.

5 Data availability

The NJIAS HCFD described in this article was released to the general public. Since the Science Data Bank accepts up to 1 TB per data publication, the NJIAS HCFD–0.04Deg was divided into four parts and published at <https://doi.org/10.57760/sciencedb.09950> (Zhuge, 2023a), <https://doi.org/10.57760/sciencedb.09953> (Zhuge, 2023b), <https://doi.org/10.57760/sciencedb.09954> (Zhuge, 2023c), and <https://doi.org/10.57760/sciencedb.10158> (Zhuge, 2023d). The NJIAS HCFD–TyWNP is published at <https://doi.org/10.57760/sciencedb.09945> (Zhuge, 2023e).

6 Summary and conclusions

To supplement the JAXA Himawari-8/9 official cloud products, which are daytime only, a dataset named the NJIAS HCFD was constructed. The NJIAS HCFD provides 30 variables (e.g., cloud mask, cloud-top phase, CTH, τ and Re , as well as snow, dust and haze masks) and covers a vast majority of the East Asia and WNP regions over the 7 yr period from April 2016 to December 2022. In this study, the NJIAS HCFD data quality has been evaluated against the CALIOP 1-km cloud layer product and the Collection-6.1 MYD06 dataset. The evaluation results are summarized as follows.

1) The POD and FAR of the NJIAS HCFD for cloud detections are ~85% and ~6%, respectively. The NJIAS HCFD gives higher skill scores than the MYD06 during nighttime over land. For other scenarios, the NJIAS HCFD lags behind the MYD06, but outperforms JAXA dataset.

2) The three cloud height parameters (CTT, CTH and CTP) of the NJIAS HCFD agree well with the MYD06 retrievals, without noteworthy underestimation or overestimation. The JAXA products show a tendency to overestimate the CTT and underestimate the CTH of high clouds.

3) The PODs of the NJIAS phase determinations for the CALIOP liquid-water and ROI cloud tops



are 81.6% (81.1%) and 88.2% (85.0) over ocean (land), respectively. Problems are found for the MYD06 and JAXA retrievals, such as misclassifying pixels with a CTT greater than 0°C as ice phase over ocean, and misclassifying pixels with a CTT below -40°C as non-ice phase over land.

4) Overall, the NJIAS DCOMP retrievals have high correlations with the Collection-6.1 MYD06 results, with CC ranging from 0.722 to 0.853. The JAXA dataset only provides Re values retrieved from the AHI 2.3- μm channel. However, the overestimation in the NJIAS $\text{Re}_{2.3}$ retrievals is not found in the JAXA retrievals.

It is anticipated that the NJIAS HCFD will play an important role in monitoring the evolutions of convection and weather systems, studying aerosol-cloud-precipitation-climate interactions, and evaluating cloud parameterization schemes in weather/climate models. Two examples presented in this article demonstrate the use of the NJIAS HCFD for climate and typhoon research. In the future, the time period of the dataset will be extended continuously. More cloud variables, such as cloud-base height and nighttime optical/microphysical parameters, may be added to the dataset by using the deep-learning-based cloud retrieval algorithms recently developed by Wang et al. (2022, 2023).

Author contributions. XZ (Xiaoyong Zhuge) conceived the idea and prepared the data. XZ (Xiaoyong Zhuge), XZ (Xiaolei Zou) and LY drafted the manuscript. All authors contributed to manuscript revisions.

Competing interests. The authors declare that they have no conflict of interests.

Acknowledgements. JAXA distributes the Himawari-8/9 raw data and level-2 cloud products (<https://www.eorc.jaxa.jp/ptree/>). NASA's official website (<https://earthdata.nasa.gov/>) provides the MYD06 and CALIOP cloud products. The authors also thank the editors and anonymous reviewers for their helpful comments and valuable suggestions, which improved the manuscript.

Financial support. This work was financially supported by the National Natural Science Foundation of China (42175006), the Fengyun Application Pioneering Project (FY-APP-2021.0101), Jiangsu Youth Talent Promotion Project (2021-084), and the Basic Research Fund of CAMS (2020R002, 2021Z002, 2021Y013, 2021Y014).

References

Avery, M. A., Ryan, R. A., Getzewich, B. J., Vaughan, M. A., Winker, D. M., Hu, Y., Garnier, A., Pelon, J., and Verhappen, C. A.: CALIOP V4 cloud thermodynamic phase assignment and the impact of



- near-nadir viewing angles, *Atmos. Meas. Tech.*, 13, 4539–4563, <https://doi.org/10.5194/amt-13-4539-2020>, 2020.
- Baum, B. A., Menzel, W., Frey, R., Tobin, D., Holz, R., Ackerman, S., Heidinger, A., and Yang, P.: MODIS Cloud-Top Property Refinements for Collection 6, *J. Appl. Meteor. Climatol.*, 1145–1163, 600 <https://doi.org/10.1175/JAMC-D-11-0203.1>, 2012.
- Baum, B. A., Yang, P., Heymsfield, A. J., Bansemmer, A., Merrelli, A., Schmitt, C., and Wang, C.: Ice cloud bulk single-scattering property models with the full phase matrix at wavelengths from 0.2 to 100 μm , *J. Quant. Spectrosc. Radiat. Transfer*, 146, 123–139, <https://doi.org/10.1016/j.jqsrt.2014.02.029>, 2014.
- 605 Bessho, K., Date, K., Hayashi, M., Ikeda, A., Imai, T., Inoue, H., Kumagai, Y., Miyakawa, T., Murata, H., Ohno, T., Okuyama, A., Oyama, R., Sasaki, Y., Shimazu, Y., Shimoji, K., Sumida, Y., Suzuki, M., Taniguchi, H., Tsuchiyama, H., Uesawa, D., Yokota, H., and Yoshida, R.: An Introduction to Himawari-8/9—Japan’s New-Generation Geostationary Meteorological Satellites, *J. Meteorol. Soc. Jpn.*, 94, 151–183, <https://doi.org/10.2151/jmsj.2016-009>, 2016.
- 610 Cai, D., Tao, L., Yang, X., Sang, X., Fang, J., Sun, X., Wang, W., and Yan H.: A climate perspective of the quasi-stationary front in southwestern China: structure, variation and impact, *Clim. Dyn.*, 59, 547–560, <https://doi.org/10.1007/s00382-022-06151-1>, 2022.
- Calvert, C., and Pavolonis, M. J.: GOES-R Advanced Baseline Imager (ABI) Algorithm Theoretical Basis Document for Low Cloud and Fog (Version 1.0), 78 pp., 615 https://www.star.nesdis.noaa.gov/goesr/documents/ATBDs/Baseline/ATBD_GOES-R_Fog_v1.0_Sep2010.pdf, 2010.
- Chen, L., Zhuge, X., Tang, X., Song, J., and Wang, Y.: A new type of red-green-blue composite and its application in tropical cyclone center positioning, *Remote Sens.*, 14, 539, <https://doi.org/10.3390/rs14030539>, 2022.
- 620 Emde, C., Buras-Schnell, R., Kylling, A., Mayer, B., Gasteiger, J., Hamann, U., Kylling, J., Richter, B., Pause, C., Dowling, T., and Bugliaro, L.: The libRadtran software package for radiative transfer calculations (version 2.0.1), *Geosci. Model Dev.*, 9, 1647–1672, <https://doi.org/10.5194/gmd-9-1647-2016>, 2016.
- Han, Y., Weng, F., Liu, Q., and van Delst, P.: A fast radiative transfer model for SSMIS upper 625 atmosphere sounding channels, *J. Geophys. Res.*, 112, D11121, <https://doi.org/10.1029/2006JD008208>, 2007.
- Heidinger, A. K.: GOES-R Advanced Baseline Imager (ABI) Algorithm Theoretical Basis Document for Cloud Height (Version 3.0), 79 pp., [https://www.star.nesdis.noaa.gov/goesr/documents/ATBDs/Baseline/ATBD_GOES-](https://www.star.nesdis.noaa.gov/goesr/documents/ATBDs/Baseline/ATBD_GOES-R_Cloud_Height_v3.0_Jul2012.pdf) 630 [R_Cloud_Height_v3.0_Jul2012.pdf](https://www.star.nesdis.noaa.gov/goesr/documents/ATBDs/Baseline/ATBD_GOES-R_Cloud_Height_v3.0_Jul2012.pdf), 2012.
- Heidinger, A.K., and Straka, W. C. III: GOES-R Advanced Baseline Imager (ABI) Algorithm Theoretical Basis Document for Cloud Mask (Version 3.0), 104 pp., [https://www.star.nesdis.noaa.gov/goesr/documents/ATBDs/Baseline/ATBD_GOES-](https://www.star.nesdis.noaa.gov/goesr/documents/ATBDs/Baseline/ATBD_GOES-R_Cloud_Mask_v3.0_Jul2012.pdf) [R_Cloud_Mask_v3.0_Jul2012.pdf](https://www.star.nesdis.noaa.gov/goesr/documents/ATBDs/Baseline/ATBD_GOES-R_Cloud_Mask_v3.0_Jul2012.pdf), 2013.



- 635 Heymsfield, A. J., Schmitt, C., and Bansemmer, A.: Ice cloud particle size distributions and pressure dependent terminal velocities from in situ observations at temperatures from 0° to -86°C, *J. Atmos. Sci.*, 70, 4123–4154, <https://doi.org/10.1175/JAS-D-12-0124.1>, 2013.
- Holmlund, K., Grandell, J., Schmetz, J., Stuhlmann, R., Bojkov, B., Munro, R., Lekouara, M., Coppens, D., Viticchie, B., August, T., Theodore, B., Watts, P., Dobber, M., Fowler, G., Bojinski, S., Schmid, A., Salonen, K., Tjemkes, S., Aminou, D., and Blythe, P.: Meteosat Third Generation (MTG): Continuation and Innovation of Observations from Geostationary Orbit, *B. Am. Meteorol. Soc.*, 102, E990–E1015, <https://doi.org/10.1175/BAMS-D-19-0304.1>, 2021.
- 640 Hu, Y., Winker, D., Vaughan, M., Lin, B., Omar, A., Trepte, C., Flittner, D., Yang, P., Nasiri, S., Baum, B., Holz, R., Sun, W., Liu, Z., Wang, Z., Young, S., Stamnes, K., Huang, J., and Kuehn, R.: CALIPSO/CALIOP cloud phase discrimination algorithm, *J. Atmos. Ocean. Technol.*, 26, 2293–2309, <https://doi.org/10.1175/2009JTECHA1280.1>, 2009.
- 645 Hutchison, K. D., Iisager, B. D., Kopp, T. J., and Jackson, J. M.: Distinguishing Aerosols from Clouds in Global, Multispectral Satellite Data with Automated Cloud Classification Algorithms, *J. Atmos. Oceanic Technol.*, 25, 501–518. <https://doi.org/10.1175/2007JTECHA1004.1>, 2008.
- 650 Ishida, H., and Nakajima, T. Y.: Development of an unbiased cloud detection algorithm for a spaceborne multispectral imager, *J. Geophys. Res. Atmos.*, 114, 1291–1298, <https://doi.org/10.1029/2008JD010710>, 2009.
- Kalnay, E., Kanamitsu, M., Kistler, R., Collins, W., Deaven, D., Gandin, L., Iredell, M., Saha, S., White, G., Woollen, J., Zhu, Y., Chelliah, M., Ebisuzaki, W., Higgins, W., Janowiak, J., Mo, K. C., Ropelewski, C., Wang, J., Leetmaa, A., Reynolds, R., Jenne, R., and Joseph, D.: The NCEP/NCAR 655 40-year reanalysis project, *B. Am. Meteorol. Soc.*, 77, 437–470, [https://doi.org/10.1175/1520-0477\(1996\)077<0437:TNYRP>2.0.CO;2](https://doi.org/10.1175/1520-0477(1996)077<0437:TNYRP>2.0.CO;2), 1996.
- Kawamoto, K., Nakajima, T., and Nakajima, T. Y.: A global determination of cloud microphysics with AVHRR remote sensing, *J. Climate*, 14, 2054–2068, [https://doi.org/10.1175/1520-0442\(2001\)014<2054:AGDOCM>2.0.CO;2](https://doi.org/10.1175/1520-0442(2001)014<2054:AGDOCM>2.0.CO;2), 2001.
- 660 Khanal, S., and Wang, Z.: Uncertainties in MODIS-based cloud liquid water path retrievals at high latitudes due to mixed-phase clouds and cloud top height inhomogeneity, *J. Geophys. Res.-Atmos.*, 123, 11154–11172. <https://doi.org/10.1029/2018JD028558>, 2018.
- Korolev, A., McFarquhar, G., Field, P. R., Franklin, C., Lawson, P., Wang, Z., Williams, E., Abel, S. J., Axisa, D., Borrmann, S., Crosier, J., Fugal, J., Krämer, M., Lohmann, U., Schlenker, O., Schnaiter, M., and Wendisch, M.: Mixed-Phase Clouds: Progress and Challenges, *Meteorol. Monographs*, 58, 5.1–5.50, <https://doi.org/10.1175/amsmonographs-d-17-0001.1>, 2017.
- 665 Lensky, I., and Rosenfeld, D.: Clouds-aerosols-precipitation satellite analysis tool (CAPSAT), *Atmos. Chem. Phys.*, 8, 6739–6753, <https://doi.org/10.5194/acp-8-6739-2008>, 2008.
- 670 Letu, H., Nagao, T. K., Nakajima, T. Y., Riedi, J., Ishimoto, H., Baran, A. J., Shang, H., Sekiguchi, M., and Kikuchi, M.: Ice cloud properties from Himawari-8/AHI next-generation geostationary satellite: Capability of the AHI to monitor the DC cloud generation process, *IEEE Trans. Geosci. Remote Sens.*, 57, 3229–3239, <https://doi.org/10.1109/TGRS.2018.2882803>, 2019.



- 675 Letu, H., Yang, K., Nakajima, T. Y., Ishimoto, H., Nagao, T. M., Riedi, J., Baran, A. J., Ma, R., Wang,
T., Shang, H., Khatri, P., Chen, L., Shi, C., and Shi, J.: High-resolution retrieval of cloud
microphysical properties and surface solar radiation using Himawari-8/AHI next-generation
geostationary satellite, *Remote Sens. Environ.*, 239, 111583,
<https://doi.org/10.1016/j.rse.2019.111583>, 2020.
- 680 Liu, C.-Y., Chiu, C.-H., Lin, P.-H., and Min, M.: Comparison of cloud-top property retrievals from
Advanced Himawari Imager, MODIS, CloudSat/CPR, CALIPSO/CALIOP, and radiosonde, *J.
Geophys. Res. Atmos.*, 125, e2020JD032683, <https://doi.org/10.1029/2020JD032683>, 2020.
- Lu, X., Yu, H., Ying, M., Zhao, B., Zhang, S., Lin, L., Bai, L., and Wan, R.: Western North Pacific
tropical cyclone database created by the China Meteorological Administration, *Adv. Atmos. Sci.*,
38, 690–699, <https://doi.org/10.1007/s00376-020-0211-7>, 2021.
- 685 Mayer, B. and Kylling, A.: Technical note: The libRadtran software package for radiative transfer
calculations - description and examples of use, *Atmos. Chem. Phys.*, 5, 1855–1877,
<https://doi.org/10.5194/acp-5-1855-2005>, 2005.
- Minnis, P., and P. Heck: GOES-R Advanced Baseline Imager (ABI) Algorithm Theoretical Basis
Document for Nighttime Cloud Optical Depth, Cloud Particle Size, Cloud Ice Water Path, and
690 Cloud Liquid Water Path (Version 3.0), 85 pp.,
[https://www.star.nesdis.noaa.gov/goesr/documents/ATBDs/Baseline/ATBD_GOES-
R_Cloud_NCOMP_v3.0_Jul2012.pdf](https://www.star.nesdis.noaa.gov/goesr/documents/ATBDs/Baseline/ATBD_GOES-R_Cloud_NCOMP_v3.0_Jul2012.pdf), 2012.
- Nakajima, T., and King, M. D.: Determination of the Optical Thickness and Effective Particle Radius of
Clouds from Reflected Solar Radiation Measurements. Part I: Theory, *J. Atmos. Sci.*, 47, 1878–
695 1893. [https://doi.org/10.1175/1520-0469\(1990\)047<1878:DOTOTA>2.0.CO;2](https://doi.org/10.1175/1520-0469(1990)047<1878:DOTOTA>2.0.CO;2), 1990.
- Nakajima, T. Y., and Nakajima, T.: Wide-Area Determination of Cloud Microphysical Properties from
NOAA AVHRR Measurements for FIRE and ASTEX Regions, *J. Atmos. Sci.*, 52, 4043–4059,
[https://doi.org/10.1175/1520-0469\(1995\)052<4043:WADOCM>2.0.CO;2](https://doi.org/10.1175/1520-0469(1995)052<4043:WADOCM>2.0.CO;2), 1995.
- Nakajima, T. Y., Tsuchiya, T., Ishida, H., Matsui, T. N., and Shimoda, H.: Cloud detection performance
700 of spaceborne visible-to-infrared multispectral imagers, *Appl. Opt.*, 50, 2601–2616,
<https://doi.org/10.1364/AO.50.002601>, 2011.
- Pavolonis, M. J.: GOES-R Advanced Baseline Imager (ABI) Algorithm Theoretical Basis Document for
Cloud Type and Cloud Phase (Version 2.0), 85 pp.,
[https://www.star.nesdis.noaa.gov/goesr/documents/ATBDs/Baseline/ATBD_GOES-
705 R_Cloud_Phase_Type_v2.0_Sep2010.pdf](https://www.star.nesdis.noaa.gov/goesr/documents/ATBDs/Baseline/ATBD_GOES-R_Cloud_Phase_Type_v2.0_Sep2010.pdf), 2010.
- Platnick, S., King, M. D., Ackerman, S. A., Menzel, W. P., Baum, B. A., Riedi, J. C., and Frey, R. A.:
The MODIS cloud products: algorithms and examples from Terra, *IEEE Trans. Geosci. Remote
Sens.*, 41, 459–473, <https://doi.org/10.1109/TGRS.2002.808301>, 2003.
- Platnick, S., Meyer, K., Wind, G., Holz, R. E., Amarasinghe, N., Hubanks, P. A., Marchant, B., Dutcher,
710 S., and Veglio, P.: The NASA MODIS-VIIRS Continuity Cloud Optical Properties Products,
Remote Sens., 13, 2, <https://doi.org/10.3390/rs13010002>, 2021.
- Platnick, S., Meyer, K. G., Wind, G., Amarasinghe, N., Wang, C., and Marchant, B.: EOS MODIS and
SNPP VIIRS Cloud Properties: User Guide for the Climate Data Record Continuity Level-2 Cloud



- 715 Top and Optical Properties Product (CLDPROP) (Version 1.0), 65 pp., <https://atmosphere-imager.gsfc.nasa.gov/sites/default/files/ModAtmo/EOSSNPPCloudOpticalPropertyContinuityProductUserGuidev1.pdf>, 2019.
- Schmit, T., Griffith, P., Gunshor, M., Daniels, J., Goodman, S., and Lehair, W.: A Closer Look at the ABI on the GOES-R Series, *B. Am. Meteorol. Soc.*, 98, 681–698, <https://doi.org/10.1175/BAMS-D-15-00230.1>, 2017.
- 720 Rosenfeld, D., Andreae, M. O., Asmi, A., Chin, M., de Leeuw, G., Donovan D. P., Kahn, R., Kinne, S., Kivekäs, N., Kulmala, M., Lau, W., Schmidt, K. S., Suni, T., Wagner, T., Wild, M., and Quaas, J.: Global observations of aerosol-cloud-precipitation-climate interactions, *Rev. Geophys.*, 52, 750–808, <https://doi.org/10.1002/2013RG000441>, 2014.
- Rossow, W. B., and Schiffer R. A.: Advances in understanding clouds from ISCCP, *B. Am. Meteorol. Soc.*, 80, 2261–2288, [https://doi.org/10.1175/1520-0477\(1999\)080<2261:AIUCFI>2.0.CO;2](https://doi.org/10.1175/1520-0477(1999)080<2261:AIUCFI>2.0.CO;2), 1999.
- 725 Stephens, G.: Radiation profiles in extended water clouds, II: Parameterization schemes, *J. Atmos. Sci.*, 35, 2123–2132, [https://doi.org/10.1175/1520-0469\(1978\)035<2123:RPIEWC>2.0.CO;2](https://doi.org/10.1175/1520-0469(1978)035<2123:RPIEWC>2.0.CO;2), 1978.
- Stephens, G.: Cloud feedbacks in the climate system: A critical review, *J. Climate*, 18, 237–273, <https://doi.org/10.1175/JCLI-3243.1>, 2005.
- 730 Stephens, G., Vane, D., Boain, R., Mace, G., Sassen, K., Wang, Z., Illingworth, A., O’connor, E., Rossow, W., Durden, S., Miller, S., Austin, R., Benedetti, A., Mitrescu, C., and the CloudSat Science Team: The CloudSat mission and the A-train: A new dimension of space-based observations of clouds and precipitation, *B. Am. Meteorol. Soc.*, 83, 1771–1790, <https://doi.org/10.1175/BAMS-83-12-1771>, 2002.
- 735 Stevens, B., and Bony, S.: What Are Climate Models Missing?, *Science*, 340, 1053–1054, <https://doi.org/10.1126/science.1237554>, 2013.
- Sun, L., Tang, X., Zhuge, X., Tan, Z., and Fang, J.: Diurnal variation of overshooting tops in typhoons detected by Himawari-8 satellite, *Geophys. Res. Lett.*, 48, e2021GL095565, <https://doi.org/10.1029/2021GL095565>, 2021.
- 740 Sun, L., Zhuge, X., and Wang, Y.: A Contour-based algorithm for automated detection of overshooting tops using satellite infrared imagery, *IEEE Trans. Geosci. Remote Sens.*, 57, 497–508, <https://doi.org/10.1109/TGRS.2018.2857486>, 2019.
- Walther, A., Straka, W., Heidinger, A. K.: GOES-R Advanced Baseline Imager (ABI) Algorithm Theoretical Basis Document for Daytime Cloud Optical and Microphysical Properties (DCOMP) (Version 3.0), 66 pp., https://www.star.nesdis.noaa.gov/goesr/documents/ATBDs/Baseline/ATBD_GOES-R_Cloud_DCOMP_v3.0_Jun2013.pdf, 2013.
- 745
- Wang, J., Liu, C., Min, M., Hu, X., Lu, Q., and Husi, L.: Effects and applications of satellite radiometer 2.25- μm channel on cloud property retrievals, *IEEE Trans. Geosci. Remote Sens.*, 56, 5207–5216, <https://doi.org/10.1109/TGRS.2018.2812082>, 2018.
- 750
- Wang, Q., Zhou, C., Letu, H., Zhu, Y., Zhuge, X., Liu, C., Weng, F., and Wang, M: Obtaining Cloud Base Height and Phase From Thermal Infrared Radiometry Using a Deep Learning Algorithm, *IEEE Trans. Geosci. Remote Sens.*, In Press, <https://doi.org/10.1109/TGRS.2023.3317532>, 2023.



- 755 Wang, Q., Zhou, C., Zhuge, X., Liu, C., Weng, F., and Wang, M.: Retrieval of cloud properties from thermal infrared radiometry using convolutional neural network, *Remote Sens. Environ.*, 278, 113079, <https://doi.org/10.1016/j.rse.2022.113079>, 2022.
- Winker, D. M., Hunt, W. H., and McGill, M. J.: Initial performance assessment of CALIOP, *Geophys. Res. Lett.*, 34, L19803, <https://doi.org/10.1029/2007GL030135>, 2007.
- 760 Yang, J., Zhang, Z., Wei, C., Lu, F., and Guo, Q.: Introducing the New Generation of Chinese Geostationary Weather Satellites, Fengyun-4, B. *Am. Meteorol. Soc.*, 98, 1637–1658, <https://doi.org/10.1175/BAMS-D-16-0065.1>, 2017.
- Yang, P., Bi, L., Baum, B. A., Liou, K.-N., Kattawar, G., and Mishchenko, M.: Spectrally consistent scattering, absorption, and polarization properties of atmospheric ice crystals at wavelengths from 0.2 to 100 μm , *J. Atmos. Sci.*, 70, 330–347, <https://doi.org/10.1175/JAS-D-12-039.1>, 2013.
- 765 Yang, P., Liou, K. N., Bi, L., Liu, C., Yi, B., and Baum, B. A.: On the radiative properties of ice clouds: Light scattering, remote sensing, and radiation parameterization, *Adv. Atmos. Sci.*, 32, 32–63, <https://doi.org/10.1007/s00376-014-0011-z>, 2015.
- Zhang, C., Zhuge, X., and Yu, F.: Development of a high spatiotemporal resolution cloud-type classification approach using Himawari-8 and CloudSat, *Int. J. Remote Sens.*, 40, 6464–6481, 770 <https://doi.org/10.1080/01431161.2019.1594438>, 2019.
- Zhuce, X.: NIIAS Himawari-8/9 Cloud Feature Dataset (HCFD)–0.04Deg. Part I: 2016–2017 (Version 3), Science Data Bank [data set], <https://doi.org/10.57760/sciencedb.09950>, 2023a.
- Zhuce, X.: NIIAS Himawari-8/9 Cloud Feature Dataset (HCFD)–0.04Deg. Part II: 2018–2019 (Version 3), Science Data Bank [data set], <https://doi.org/10.57760/sciencedb.09953>, 2023b.
- 775 Zhuce, X.: NIIAS Himawari-8/9 Cloud Feature Dataset (HCFD)–0.04Deg. Part III: 2020–2021 (Version 3), Science Data Bank [data set], <https://doi.org/10.57760/sciencedb.09954>, 2023c.
- Zhuce, X.: NIIAS Himawari-8/9 Cloud Feature Dataset (HCFD)–0.04Deg. Part IV: 2022–2023 (Version 3), Science Data Bank [data set], <https://doi.org/10.57760/sciencedb.10158>, 2023d.
- Zhuce, X.: NIIAS Himawari-8/9 Cloud Feature Dataset (HCFD)–TyWNP (Version 3), Science Data 780 Bank [data set], <https://doi.org/10.57760/sciencedb.09945>, 2023e.
- Zhuce, X., and Zou, X.: Test of a Modified Infrared-Only ABI Cloud Mask Algorithm for AHI Radiance Observations, *J. Appl. Meteor. Climatol.*, 55, 2529–2546, <https://doi.org/10.1175/JAMC-D-16-0254.1>, 2016.
- Zhuce, X., and Zou, X.: Summertime Convective Initiation Nowcasting over Southeastern China Based 785 on Advanced Himawari Imager Observations, *J. Meteorol. Soc. Jpn.*, 96, 337–353, <https://doi.org/10.2151/jmsj.2018-041>, 2018.
- Zhuce, X., Guan, J., Yu, F., and Wang, Y.: A New Satellite-based Indicator for Estimation of the Western North Pacific Tropical Cyclone Current Intensity, *IEEE Trans. Geosci. Remote Sens.*, 53, 5661–5676, <https://doi.org/10.1109/TGRS.2015.2427035>, 2015.
- 790 Zhuce, X., Yu, F., and Zhang, C.: Rainfall retrieval and nowcasting based on multispectral satellite images. Part I. Retrieval study on daytime 10-minute rain rate, *J. Hydrometeorol.*, 12, 1255–1270, <https://doi.org/10.1175/2011JHM1373.1>, 2011.



- Zhuge, X., Zou, X., and Wang, Y.: A Fast Cloud Detection Algorithm Applicable to Monitoring and Nowcasting of Daytime Cloud Systems, *IEEE Trans. Geosci. Remote Sens.*, 55, 6111-6119, <https://doi.org/10.1109/TGRS.2017.2720664>, 2017.
- 795
- Zhuge, X., Zou, X., and Wang, Y.: Determining AHI Cloud-Top Phase and Intercomparisons with MODIS Products over North Pacific, *IEEE Trans. Geosci. Remote Sens.*, 59, 436-448, <https://doi.org/10.1109/TGRS.2020.2990955>, 2021a.
- Zhuge, X., Zou, X., and Wang, Y.: AHI-derived Daytime Cloud Optical/Microphysical Properties and Their Evaluations with the Collection-6.1 MOD06 Product, *IEEE Trans. Geosci. Remote Sens.*, 59, 6431-6450, <https://doi.org/10.1109/TGRS.2020.3027017>, 2021b.
- 800